



HAL
open science

Multi-scale modeling of the effects of temperature, radiation flux and sink strength on point-defect and solute redistribution in dilute Fe-based alloys

Liangzhao Huang, Maylise Nastar, Thomas Schuler, Luca Messina

► **To cite this version:**

Liangzhao Huang, Maylise Nastar, Thomas Schuler, Luca Messina. Multi-scale modeling of the effects of temperature, radiation flux and sink strength on point-defect and solute redistribution in dilute Fe-based alloys. *Physical Review Materials*, 2021, 5 (3), pp.033605. 10.1103/PhysRevMaterials.5.033605 . cea-03483651

HAL Id: cea-03483651


<https://cea.hal.science/cea-03483651v1>

Submitted on 16 Dec 2021

HAL is a multi-disciplinary open access archive for the deposit and dissemination of scientific research documents, whether they are published or not. The documents may come from teaching and research institutions in France or abroad, or from public or private research centers.

L'archive ouverte pluridisciplinaire **HAL**, est destinée au dépôt et à la diffusion de documents scientifiques de niveau recherche, publiés ou non, émanant des établissements d'enseignement et de recherche français ou étrangers, des laboratoires publics ou privés.

Multiscale modeling of the effects of temperature, radiation flux, and sink strength on point-defect and solute redistribution in dilute Fe-based alloys

Liangzhao Huang ^{*}, Maylise Nastar, and Thomas Schuler

Université Paris-Saclay, CEA, Service de Recherches de Métallurgie Physique, F-91191 Gif-sur-Yvette, France

Luca Messina

CEA, DEs, IRESNE, DEC-Service d'Études et de Simulation du Comportement des Combustibles, Cadarache F-13108 Saint-Paul-Lez-Durance, France



(Received 7 August 2020; revised 20 December 2020; accepted 22 February 2021; published 15 March 2021)

In this work, we investigate the radiation-induced segregation (RIS) resulting from the coupling between the atomic and point defect (PD) fluxes toward the structural defects of the microstructure. This flux coupling depends on the migration mechanisms of PDs and atoms, including thermal diffusion mechanisms and forced atomic relocations (FAR) occurring in displacement cascades. We derive an analytic model of the PD and solute RIS profiles accounting for PD production and mutual recombination, the FAR mechanism, and the overall sink strength of the microstructure controlling the elimination of PDs at structural defects. From this model, we present a parametric investigation of diffusion and RIS properties in dilute Fe-*B* (*B* = P, Mn, Cr, Si, Ni, and Cu) binary alloys, in the form of quantitative temperature/radiation flux/sink strength maps. As in previous works, we distinguish three kinetic domains for the diffusion and RIS properties: the recombination domain, the sink domain, and the thermal domain. Both our analytical approach and numerical applications demonstrate that the diffusion and RIS behaviors of PDs and solute atoms largely differ from one kinetic domain to another. Moreover, at high radiation flux, low temperature, and large sink strength, FARs tend to destroy the solute RIS profiles and therefore reduce the overall amount of RIS by forcing the mixing of solute and host atoms, especially close to PD sinks. Finally, we provide quantitative criteria to emulate in-reactor RIS behaviors by ion irradiation.

DOI: [10.1103/PhysRevMaterials.5.033605](https://doi.org/10.1103/PhysRevMaterials.5.033605)

I. INTRODUCTION

The radiation-induced redistribution of solute atoms in materials is largely controlled by the kinetic coupling between fluxes of lattice point defects (PDs) and atomic fluxes [1]. PDs are created by irradiation in the form of Frenkel pairs consisting of a vacancy and a self-interstitial atom (SIA). They diffuse and interact with atoms and other PDs, as well as with the microstructure of the material [2]. Irradiation therefore enhances and induces redistribution of solute atoms, and affects their interplay with the microstructure, leading to strong modifications of the mechanical, corrosion, and dimensional properties of materials [2]. Long-range diffusion of atoms under irradiation is mediated by successive exchanges of atoms with nearest-neighbor PDs as well as forced atomic relocation (FAR) events taking place in a displacement cascade [2–6]. The relative importance of each diffusion mechanism depends on the nature of the irradiation particles and on the rate of particle irradiation. The number of Frenkel pairs created [or displacement per atom per second (dpa/s)] and the number of FAR events [or replacement per atom per second (rpa/s)] are proportional to the radiation flux, which enables comparison between various irradiation particles [7–9].

Under a sustained radiation flux, the steady-state creation and elimination of PDs generates net fluxes of PDs toward the extended structural defects acting as PD sinks such as

grain boundaries (GBs), dislocation lines, dislocation loops and voids. Net fluxes of PDs make solute atoms diffuse toward or away from the PDs sinks. Since the PD-solute flux coupling differs from one chemical species to another, a change of the alloy composition occurs close to the PD sinks. This is the so-called radiation-induced segregation (RIS) phenomenon [10–13]. Recently, we have shown that when the FAR frequency is close to the thermal PD jump frequency, FAR may either enhance or reduce the PD-solute flux coupling [6]. Note that both chemical species and PDs form a RIS profile at sinks. The RIS of PDs is systematically negative, with a concentration profile dropping to thermal equilibrium concentration at sinks. RIS occurs at every PD sink even at very small radiation doses [14]. Therefore, RIS is often a precursor for heterogeneous precipitation of secondary phases at PD sinks, as for example the precipitation of the ordered phase Ni₃-Si in austenitic steels [11,15], and the formation of Mn-Ni-Si-rich clusters in reactor pressure vessel ferritic steels [16–20]. RIS can induce failure of materials through various mechanisms [2,21], for instance the lowering of corrosion resistance due to depletion of chromium at GBs in austenitic steels [22], material embrittlement resulting from phosphorus enrichment at GBs [16], or the shift of the ductile-to-brittle transition temperature in reactor pressure vessel steels due to the formation of solute-rich clusters [19].

The sign of solute RIS, positive for solute enrichment and negative for solute depletion, is directly related to the relative magnitude of solute-vacancy and solute-SIA

^{*}huang.liangzhao@outlook.com

flux coupling [23]. Calculation methods of flux-coupling coefficients rely on the Onsager formulation of solute and PDs fluxes within the framework of the thermodynamics of irreversible processes [24] where these fluxes are expressed as linear combinations of chemical potential gradients. The coefficient of proportionality between the flux of species i and the gradient of the chemical potential of species j is the so-called phenomenological transport coefficient denoted L_{ij} . These transport coefficients are material specific and depend on the diffusion mechanism [12]. For a given system, the experimental measurement of all the transport coefficients is challenging and in most cases impossible. For instance, one cannot measure equilibrium diffusion properties mediated by SIA in metals because the equilibrium concentration of SIAs is too small. Furthermore, it is almost impossible to measure the off-diagonal phenomenological coefficients that are responsible for positive vacancy-solute flux coupling because these coefficients control the solute flux only when the alloying driving force is weak, which is not the case in standard thermal diffusion experiments [12]. The recent progress of first-principles methods allows us to compute these phenomenological transport coefficients from *ab initio* [23,25–27] energetics combined with statistical models of diffusion on a lattice. The L_{ij} essentially depend on the PDs diffusion mechanism and the variation of PD jump frequencies with the local alloy composition. At steady state, the RIS factor relating the solute local concentration gradients to the local PD concentration gradient normalized by the local PD concentration is essentially a function of the phenomenological coefficients L_{ij} , the concentration derivatives of chemical potentials, and the solute and PD local concentrations [12,13]. When the RIS factor is assumed to be a constant, the amplitude of the solute concentration gradient is proportional to the normalized PD concentration gradients [28]. Therefore, the amplitude and shape of the stationary RIS profile depends not only on the RIS factor, but also on the local concentration of PDs [12,28]. The evolution of the PD concentration fields depends on their mobility, the radiation flux, their mutual interaction, and their interaction with the microstructure and the solutes. Among PD reactions, let us mention the mutual recombination of vacancy and SIA, the clustering of PDs leading to the formation of dislocation loops and voids, and the elimination of PDs at sinks. The analysis of PD-microstructure interactions may be simplified by introducing an effective PD sink strength governing the average PD elimination rate at all PD sinks. However, the microstructure is in constant evolution due to PD clustering, production, elimination at sinks, and their interplay with solute reactions. It is therefore crucial to take the latter phenomena into account, but up to now, there is no modeling method able to account for the evolution of both the sink microstructure and the solute redistribution. Most of the RIS models either work at fixed concentrations of PDs [29–31], or for the most advanced ones at a fixed value of the overall PD sink strength [28,32,33].

There are experimental studies investigating the dependence of RIS on the microstructure of the irradiated sample and the irradiation conditions, including the nature of the irradiation particles [34,35], the radiation dose and dose rate [36,37], and temperature [38,39]. However, it is still very difficult to obtain an accurate estimation of the PD sink

strength from the observation of the microstructure due to the limitations of resolution, even for nanoscale experimental techniques. In order to obtain an accurate estimation of the sink strength, experimental measurements need to be complemented with modeling [40]. Predicting the evolution of RIS in nuclear power plant materials from a direct observation of neutron-irradiated materials is difficult, mainly because neutron irradiation activates the sample and the radiation exposure times of several years needed to reach a few dpa are rarely available [2]. Radiation fluxes of electrons and heavy ions can be high, which allows radiation doses to reach up to hundreds of dpa in a much shorter time. However, most of the phenomena occurring under irradiation are sensitive to the radiation flux. According to simple mean-field rate theories, the PD concentrations obtained at a low radiation flux and a given temperature are identical to the ones obtained at a higher flux provided the temperature is increased by a specific amount, which suggests that a difference in radiation flux can be compensated by a temperature shift [2,41,42]. This theory has been first applied to investigate the swelling phenomena, but it relies on the assumption that solute atoms do not interfere with the kinetics of PDs and the overall PD sink strength is fixed by the initial microstructure. According to this theory, there are three kinetic domains: (i) at low temperature and high radiation flux, the recombination domain in which the PD concentration is controlled by the PD recombination reaction; (ii) at intermediate temperature and low radiation flux, the sink domain in which the PD concentration is controlled by the elimination of PDs at sinks; and (iii) at high temperature and low radiation flux, the thermal domain in which the PD concentration is close to thermal equilibrium concentration [41]. Estimations of the temperature shift required to compensate for a large radiation flux depend on the kinetic domain of the experiment and whether the system is at steady state or in a transient state. These temperature shifts require the definition of an invariant quantity, either the bulk concentration of PDs at steady state [2] or the amount of PDs absorbed by sinks [42]. Attempts have been made to apply Mansur's invariant PD-absorption relation to the study of solute RIS [2,34,35]. The estimation of the temperature shift was good enough to yield similar RIS profiles of Cr and Ni in 304L stainless steels, respectively irradiated with neutrons and self-ions [35]. Nevertheless, in the same publication, the authors observe that the temperature shift predicted by Mansur's invariant relation is not accurate for alloys with a high dislocation density. Yet, a material with an initial high dislocation density seems to be more appropriate to test Mansur's invariant relation, because the high PD sink strength of a microstructure full of dislocations is less sensitive to the radiation flux and dose, and can be considered to be fixed as assumed in Mansur's theory. A recent analytical model of steady-state RIS in the sink domain precisely predicts that solute RIS does not depend on the radiation flux, whereas PD concentration does [28]. However, as explained by the authors, we should not ignore that an increase of the dislocation density may induce a transition from the recombination domain to the sink domain, hence, shift the system from a radiation-flux dependence to another. Therefore, there is a need for a PD-RIS model accounting for both the transitions between the various PD kinetic domains, and the effect of the irradiation conditions and the

microstructure on the RIS profile within each PD kinetic domain.

As an important step toward a fully consistent model of solute redistribution coupled with sink-strength evolution, we derive an analytical RIS model, aimed at (i) taking into account all PD reactions, solute-PD interactions, and FAR mechanisms; (ii) quantitatively studying the effect of a variation of either the sink strength, the radiation flux, or the temperature on the RIS properties; and (iii) understanding and quantifying the flux-temperature effect in experiments for each kinetic domain (recombination/sink/thermal).

To this end, we extend the analytical approach of Ref. [28] to the whole temperature/radiation flux domain by including the effect of FAR and PD recombination reactions. Furthermore, we account for the variation of the RIS factor with PD and solute concentration along the segregation profiles. Starting from the Onsager formulation [24,43], the effect of radiation damage is taken into account at different scales. At the cluster-dynamics scale, irradiation produces a supersaturation of PDs, which affects the driving forces as well as the transport coefficients. At the atomic scale, recent developments of the self-consistent mean-field theory [44,45] provide a procedure to treat the interplay between thermal PD diffusion mechanisms that satisfy the microscopic detailed balance, and the FAR diffusion mechanism that satisfies the global detailed balance only. The introduction of FAR in the self-consistent mean-field theory explains how short-range order (relative probabilities of atomic configurations) is affected by ballistic mixing, and therefore how transport coefficients are affected accordingly [6]. The resulting atomic fluxes under a steady-state gradient of concentration are still linear combinations of gradients of chemical potentials, even though the transport coefficients no longer obey the Onsager reciprocal relations, and the chemical potentials depend on FAR [6]. Relying on the implementation of these theoretical developments in the KineCluE code [46], and on the recently published DFT database of vacancy and SIA hop frequencies, we present a quantitative study of flux coupling in dilute Fe-*B* ($B = \text{P, Mn, Cr, Si, Ni, and Cu}$) binary alloys [47] with respect to radiation flux, temperature, and PD sink strength. Combining flux-coupling factors with the analytical RIS model leads to quantitative maps of RIS with respect to these parameters. Based on the analytical PD-RIS model and its application to the Fe alloys, we discuss the validity and relevance of the temperature-shift criteria in the three PD kinetic domains.

This paper is organized as follows: Sec. II is devoted to a short presentation of the methods used to compute flux-coupling coefficients and bulk concentrations of PDs at steady state, and to the derivation of our RIS analytical model. Results of diffusion and RIS properties of Fe alloys are found in Sec. III. In the first part of Sec. IV, we discuss the limitations of the model resulting from some of the assumptions, and in the second part, we show how the present model can be used to derive temperature-shift criteria. A summary, concluding remarks, and perspectives are given in Sec. V.

II. MODELS

A solute RIS profile is a complex function of the local concentrations of PDs and solute atoms, the local concentra-

tion dependent diffusion coefficients, the radiation flux, and the PD sink strength. We will present the procedure that we used to compute the diffusion coefficients, the flux-coupling coefficients (also called flux-coupling ratios), and the RIS factor from the Onsager formulation of fluxes in a binary dilute alloy A(B). The key variables that are used in the following derivation are listed in Appendix A.

A. Diffusion properties

Following the Onsager formulation, we write the fluxes of PDs and atoms as functions of the phenomenological transport coefficients and the chemical potential gradients. Then, we briefly introduce the cluster expansion of the transport coefficients. This expansion provides an explicit variation of the transport coefficients with respect to the local PD and solute concentrations and their thermodynamic interactions. From these fluxes, we introduce the flux-coupling coefficient that relates the solute flux to the PD flux in the presence of a PD chemical potential gradient. In the infinitely dilute limit—when the interactions between solute atoms, PDs, and solute-PD clusters larger than pairs are ignored—we express the chemical potential gradients in terms of concentration gradients and to obtain the expressions of partial, PD, and solute diffusion coefficients.

1. Atomic fluxes and phenomenological coefficients

Following Onsager's formalism [24,43], we express the flux J_α of species α as a linear combination of chemical potential gradients (e.g., $\nabla\mu_\beta$ for species β). We assume that fluxes arising from the vacancy (V) diffusion mechanism and from the self-interstitial atom (SIA or I) diffusion mechanism are additive. In a binary alloy A(B), the flux of atomic species α ($\alpha = A$ or B) reads

$$J_\alpha = J_\alpha^V + J_\alpha^I, \quad (1)$$

with

$$J_\alpha^V = -\frac{1}{k_B T} \sum_{\beta=A,B,V} L_{\alpha\beta}^V \nabla\mu_\beta, \quad (2)$$

$$J_\alpha^I = -\frac{1}{k_B T} \sum_{\beta=A,B,I} L_{\alpha\beta}^I \nabla\mu_\beta. \quad (3)$$

Similarly, the fluxes of vacancies and SIAs read

$$J_V = -\frac{1}{k_B T} \sum_{\beta=A,B,V} L_{V\beta}^V \nabla\mu_\beta, \quad (4)$$

$$J_I = -\frac{1}{k_B T} \sum_{\beta=A,B,I} L_{I\beta}^I \nabla\mu_\beta. \quad (5)$$

In Eqs. (2), (3), (4), and (5), the coefficients $L_{\alpha\beta}^V$ and $L_{\alpha\beta}^I$ are the phenomenological transport coefficients that characterize the diffusion mediated respectively by vacancies and SIAs. For the sake of simplicity, $L_{\alpha V}^V$ and $L_{\alpha I}^I$ are respectively denoted $L_{\alpha V}$ and $L_{\alpha I}$.

By using the self-consistent mean-field theory, we compute the transport coefficients from the atomic jump frequencies [44,45]. This theory has been applied to quantitative studies of vacancy-mediated diffusion properties [23,26,27,48,49], combined with the direct interstitial migration mechanism

[49,50], and the SIA diffusion mechanism in dilute [47,51] and concentrated alloys [52]. It has also been extended to diffusion mechanisms that do not satisfy the microscopic detailed balance such as the FAR mechanism [6]. The recent development of a cluster formulation of the self-consistent mean field theory and its implementation into the KineCluE code [46] allows for systematic and sensitivity studies of the solute concentration, strain, and temperature effects on transport coefficients in multicomponent alloys [26,47,49].

Now we introduce the vacancy and SIA diffusion mechanisms, as well as the FAR diffusion mechanism. The latter models the effect of athermal ballistic mixing on atoms and defects. According to the parametric study of the effect of FAR on transport coefficients, at most irradiation conditions in bcc iron alloys, varying the range of FAR does not fundamentally change the diffusion properties, in particular the flux-coupling coefficients [6]. Therefore, for the sake of simplicity, we restrict the FAR mechanism to forced exchanges of atoms with their first nearest neighbors (1-NN) that can be either an atom of a different chemical species or a vacancy. Note that a purely random FAR mechanism is equivalent to a ballistic mixing event. In the present study, we ignore the FAR events with SIAs because FAR frequencies are always negligible compared to SIA thermal jump frequencies. For each Frenkel pair created, the number of FAR events, n_{FAR} , ranges from a few units for electron irradiation to several hundreds for neutron irradiation [3]. The contribution of the FAR mechanism to the atomic transport increases with n_{FAR} . In the following, we set $n_{\text{FAR}} = 100$ unless specified otherwise.

In a dilute binary alloy A(B), we consider five different cluster configurations. The B- d pair configurations correspond to a single PD ($d = \text{V}$ or I) bound to a single solute atom B up to a distance lower than a kinetic radius R_k . Whenever the distance between B and d is larger than R_k , we consider B and d as isolated monomers. Therefore, the five cluster contributions considered here are the three monomers B, V, and I and the two pairs B-V and B-I. We use the code KineCluE [46] to compute the transport coefficients of each cluster from the *ab initio* atomic jump frequencies. Following the kinetic cluster expansion formulation of the transport coefficients in dilute alloys, we deduce the overall transport coefficients from the cluster transport coefficients [46]

$$\begin{aligned} L_{\text{BB}}^d &= L_{\text{BB}}^{d,\text{pair}} C_{\text{Bd}}^{\text{pair}} + L_{\text{BB}}^{\text{mono}} C_{\text{B}}^{\text{mono}}, \\ L_{dd} &= L_{dd}^{\text{pair}} C_{\text{Bd}}^{\text{pair}} + L_{dd}^{\text{mono}} C_d^{\text{mono}}, \\ L_{\text{Bd}} &= L_{\text{Bd}}^{\text{pair}} C_{\text{Bd}}^{\text{pair}}, \\ L_{d\text{B}} &= L_{d\text{B}}^{\text{pair}} C_{\text{Bd}}^{\text{pair}}. \end{aligned} \quad (6)$$

Note that the cluster transport coefficients ($L_{\alpha\beta}^{\text{pair}}$ and $L_{\alpha\beta}^{\text{mono}}$) are intrinsic cluster properties that do not depend on the local atomic fraction C_α of species $\alpha = \{\text{A}, \text{B}, d\}$, while the overall transport coefficients do. The cluster atomic fractions $C_{\text{Bd}}^{\text{pair}}$, C_d^{mono} , and $C_{\text{B}}^{\text{mono}}$ are deduced from C_α , and are computed in the framework of low-temperature expansions [53–55]. In most irradiation conditions of interest, $C_d \ll C_{\text{B}}$. Therefore,

the cluster atomic fractions are given by [47]

$$\begin{aligned} C_{\text{Bd}}^{\text{pair}} &= \frac{C_{\text{B}} C_d Z_{\text{Bd}}}{Z_d + C_{\text{B}}(Z_{\text{Bd}} - Z_{\text{Bd}}^0)}, \\ C_d^{\text{mono}} &= C_d \left[1 - \frac{C_{\text{B}} Z_{\text{Bd}}}{Z_d + C_{\text{B}}(Z_{\text{Bd}} - Z_{\text{Bd}}^0)} \right], \\ C_{\text{B}}^{\text{mono}} &= C_{\text{B}}, \end{aligned} \quad (7)$$

where Z_{Bd} is the partition function of the pair B- d , Z_{Bd}^0 is the number of pair configurations, $Z_{\text{V}} = 1$ for vacancies, and $Z_{\text{I}} = 6$ for $\langle 110 \rangle$ dumbbells. In this case, L_{dd} , L_{Bd} , and $L_{d\text{B}}$ are proportional to C_d whereas L_{BB}^d can be decomposed into two parts, the first being proportional to C_d and the other one independent of C_d . Note that the coefficient $L_{\text{BB}}^{\text{mono}}$ is zero unless the FAR mechanism is included, because under equilibrium conditions a substitutional solute requires the presence of PDs to diffuse.

2. Flux-coupling coefficients

To investigate the flux coupling driven by an excess of vacancy or SIA, we consider the ratio between fluxes of V (respectively SIA) and solute atoms (B) in a binary alloy A(B). Before irradiation, solute atoms are mostly at local equilibrium in the vicinity of PD sinks; i.e., their gradient of chemical potential is zero. From its very beginning, irradiation produces an excess of PDs which increases as we move away from PD sinks, leading to a gradient of PD chemical potential. Therefore, $\nabla\mu_{\text{V}}$ (respectively $\nabla\mu_{\text{I}}$) are the main diffusion driving forces, at least at the beginning of irradiation. In order to investigate the flux coupling induced by these PD driving forces, we set to zero all the other gradients of chemical potential. Hence, $J_{\text{V}}/J_{\text{B}}$ and $J_{\text{I}}/J_{\text{B}}$ are respectively given by the flux-coupling coefficients [39,56,57]:

$$\delta_{\text{V}} = \frac{L_{\text{BV}}}{L_{\text{VV}}} \quad (8)$$

for the B-V coupling and

$$\delta_{\text{I}} = \frac{L_{\text{BI}}}{L_{\text{II}}} \quad (9)$$

for the B-SIA coupling.

These factors δ_{V} and δ_{I} give the average number of solute atoms dragged by a vacancy and an SIA, respectively. Note that L_{VV} , L_{II} , and L_{BI} are systematically positive, while L_{BV} may be negative. The off-diagonal coefficient L_{BV} determines the sign of the B-V flux coupling. When $\delta_{\text{V}} < 0$, the atom flux is on average opposite to the vacancy flux. When $\delta_{\text{V}} > 0$, vacancies drag solute atoms toward PD sinks through correlated sequences of solute-vacancy exchanges. Note that when the atomic relocation frequency of the FAR mechanism is close to the thermal jump frequency, the flux coupling is reduced in magnitude [6].

3. Partial and intrinsic diffusion coefficients

At most irradiation conditions in experiments (typically at $T > 300$ K and a dose rate $\phi < 0.01$ dpa/s), PDs can be considered as dilute species due to their relatively low concentrations, even though these concentrations can be orders of magnitude higher than equilibrium PD concentrations. Thus,

we choose to ignore the effect of thermodynamic and kinetic interactions between PDs on any diffusion properties. Furthermore, we limit the study to infinitely dilute binary alloys A(B), meaning that we ignore thermodynamic and kinetic interactions between solute atoms B. Therefore, in the A(B) binary alloy with a single type of PD (either V or SIA), the transport coefficients are linear functions of the point defect concentration. To highlight the dependency of the transport coefficients upon the PD concentrations, normalized transport coefficients are introduced, the so-called partial diffusion coefficients [12,29,30,32], which are independent of PD concentration:

$$\begin{aligned} d_{AV} &= -\frac{L_{AA}^V + L_{AB}^V}{C_A C_V}, & d_{BV} &= -\frac{L_{BB}^V + L_{BA}^V}{C_B C_V}, \\ d_{AI} &= \frac{L_{AA}^I + L_{AB}^I}{C_A C_I}, & d_{BI} &= \frac{L_{BB}^I + L_{BA}^I}{C_B C_I}, \\ d_{AV}^c &= \frac{L_{AA}^V}{C_A C_V} - \frac{L_{AB}^V}{C_B C_V} + d_{AV} \frac{1}{\Phi} \xi_{VA}, \\ d_{BV}^c &= \frac{L_{BB}^V}{C_B C_V} - \frac{L_{BA}^V}{C_A C_V} + d_{BV} \frac{1}{\Phi} \xi_{VB}, \\ d_{AI}^c &= \frac{L_{AA}^I}{C_A C_I} - \frac{L_{AB}^I}{C_B C_I} + d_{AI} \frac{1}{\Phi} \xi_{IA}, \\ d_{BI}^c &= \frac{L_{BB}^I}{C_B C_I} - \frac{L_{BA}^I}{C_A C_I} + d_{BI} \frac{1}{\Phi} \xi_{IB}, \end{aligned} \quad (10)$$

where Φ is the thermodynamic factor [12], $\xi_{d\alpha} = (\partial \ln C_d^{\text{eq}})/(\partial \ln C_\alpha)$, and C_d^{eq} is the equilibrium PD concentration. Since multiple-solute and multiple-defect effects are neglected in the dilute-limit approximation, Φ is equal to 1, and the factors $\xi_{d\alpha}$ are assumed to be zero. Moreover, transport coefficients and intrinsic diffusion coefficients are related by

$$D_\beta = d_{\beta V}^c C_V + d_{\beta I}^c C_I, \quad \beta \in \{A, B\}. \quad (11)$$

Combining Eqs. (6), (7), and (11), D_β is rewritten as

$$D_\beta = d_{\beta V}^{c,0} C_V + d_{\beta I}^{c,0} C_I + L_{BB}^{\text{mono}}, \quad \beta \in \{A, B\}, \quad (12)$$

where $d_{\beta d}^{c,0}$ is given by

$$d_{Ad}^{c,0} = \left(\frac{L_{AA}^{d,\text{pair}}}{C_A C_d} - \frac{L_{AB}^{d,\text{pair}}}{C_B C_d} \right) C_{Bd}^{\text{pair}}, \quad (13)$$

$$d_{Bd}^{c,0} = \left(\frac{L_{BB}^{d,\text{pair}}}{C_B C_d} - \frac{L_{BA}^{d,\text{pair}}}{C_A C_d} \right) C_{Bd}^{\text{pair}}. \quad (14)$$

Note that L_{BB}^{mono} is independent of PD concentrations.

Finally, we express the diffusion coefficients of vacancies (D_V) and SIAs (D_I) in terms of transport coefficients

$$D_V = \frac{L_{VV}}{C_V} \quad \text{and} \quad D_I = \frac{L_{II}}{C_I}. \quad (15)$$

B. Concentration profiles of point defects at sinks

The sustained creation of PDs under irradiation and their elimination at sinks leads to a steady-state depleted concentration profile of PDs at sinks. By analogy with the solute

RIS, we call it the RIS profile of PDs. We introduce an analytical method to calculate this concentration profile. First, we derive the bulk concentration of PDs at steady state from standard mean-field rate theory [41]. Then, we calculate the steady-state profile by splitting the PD concentration profile into two parts and then integrating the flux of PDs.

1. Rate theory

The concentration of PDs varies under irradiation, mainly due to the production of Frenkel pairs, the mutual recombination between SIA and vacancy, and the elimination of PDs at sinks. We deduce the time derivative of the bulk concentration of PDs $d = \{V, I\}$ under irradiation C_d^b from a classic rate-theory model [1,41,54]

$$\frac{dC_d^b}{dt} = \phi - K_R C_V^b C_I^b - K_d (C_d^b - C_d^{\text{eq}}), \quad (16)$$

where $K_R = (4\pi r_c/\Omega)(D_I + D_V)$ stands for the SIA-V recombination rate whereas $K_V = k_V^2 D_V$ and $K_I = k_I^2 D_I$ correspond respectively to the elimination rate of vacancies and SIAs at PD sinks. At PD sinks, we assume that local equilibrium is established and concentrations of PDs correspond to the equilibrium ones. r_c is the SIA-V recombination radius, usually assumed to be in the same order of magnitude as the lattice parameter a_0 . Ω is the atomic volume, ϕ the radiation dose rate, i.e., the PD production rate, while k_V^2 and k_I^2 are the sink strength respectively for vacancies and SIAs. We assume that the PD sinks are neutral (i.e., any sink bias is neglected), hence $k_V^2 = k_I^2 = k^2$. Note that $k^2 = \sum_s k_s^2$ is the total sink strength, which is summed up over all contributions of the various PD sinks (k_s^2). In steady state, we have

$$D_V (C_V^b - C_V^{\text{eq}}) = D_I (C_I^b - C_I^{\text{eq}}). \quad (17)$$

Note that, in general, SIAs diffuse much faster than vacancies (i.e., $D_I \gg D_V$) [2]. Furthermore, the equilibrium SIA concentration C_I^{eq} in metals is in general negligible with respect to C_V^b [2]. Therefore, the steady-state solution of Eq. (16) for C_V^b is given by

$$C_V^b = \frac{C_V^{\text{eq}}}{2} - \frac{k^2 \Omega}{8\pi r_c} + \sqrt{\left(\frac{C_V^{\text{eq}}}{2} + \frac{k^2 \Omega}{8\pi r_c} \right)^2 + \frac{\Omega}{4\pi r_c} \left(\frac{\phi}{D_V} \right)}, \quad (18)$$

and the general solution for C_I^b is obtained from Eq. (17). By applying the low-temperature expansion formalism [6,53–55] to the infinitely dilute binary alloy A(B) at equilibrium, we have

$$C_V^{\text{eq}} = C_V^{\text{eq},0} \left[1 + \frac{(Z_{BV} - Z_{BV}^0) \bar{C}_B}{1 + (Z_{BV} - Z_{BV}^0) C_V^{\text{eq},0}} \right], \quad (19)$$

where \bar{C}_B is the nominal concentration of solute atoms B and $C_V^{\text{eq},0}$ is the equilibrium concentration in pure metal obtained from the vacancy formation enthalpy H_V^f and entropy S_V^f by

$$C_V^{\text{eq},0} = \exp\left(-\frac{H_V^f - T S_V^f}{k_B T} \right). \quad (20)$$

Note that we may neglect C_V^{eq} with respect to C_V^b in the recombination and sink domains of PDs [2]. We will take C_V^{eq}

into account to define the transition between thermal and sink domains.

In the sink domain, the elimination of PDs at sinks is dominant versus the SIA-V recombination, i.e., $K \gg R$ with

$$K = K_V(C_V^b - C_V^{eq}) \quad \text{and} \quad R = K_R C_V^b C_I^b. \quad (21)$$

Therefore, the bulk vacancy concentration C_V^b at steady state is proportional to the ratio ϕ/D_V and given by

$$C_V^b = \frac{1}{k^2} \left(\frac{\phi}{D_V} \right). \quad (22)$$

In the recombination domain, i.e., when $K \ll R$, the vacancy concentration is proportional to $\sqrt{\phi/D_V}$, so that we have $C_V^b = C_I^b$ because Eq. (18) is not valid anymore. In this case, the bulk concentration reads

$$C_V^b = \sqrt{\frac{\Omega}{4\pi r_c} \left(\frac{\phi}{D_V} \right)}. \quad (23)$$

2. Steady-state RIS profile of point defects

Homogeneous mean-field rate theory does not provide the concentration profiles of PDs at sinks that form under sustained irradiation. From the continuity equation, we express the elimination rate of PDs as a divergence of the vacancy flux \mathbf{J}_V and the SIA flux \mathbf{J}_I :

$$\frac{\partial C_V}{\partial t} = \phi - K_R C_V C_I - \nabla \cdot \mathbf{J}_V, \quad (24)$$

$$\frac{\partial C_I}{\partial t} = \phi - K_R C_V C_I - \nabla \cdot \mathbf{J}_I. \quad (25)$$

To compute \mathbf{J}_V and \mathbf{J}_I , we assume $\nabla\mu_V$ and $\nabla\mu_I$ to be the dominant driving forces compared to $\nabla\mu_A$ and $\nabla\mu_B$. Moreover, we neglect the variation of the equilibrium point defect concentration along the solute RIS profile (see Appendix B). Thus, we have

$$\mathbf{J}_V = -\frac{L_{VV}}{k_B T} \nabla\mu_V = -D_V \nabla C_V, \quad (26)$$

$$\mathbf{J}_I = -\frac{L_{II}}{k_B T} \nabla\mu_I = -D_I \nabla C_I. \quad (27)$$

We present the calculation of the PD concentration profile in a one-dimensional symmetric system delimited by two planar sinks parallel to each other, as illustrated in Fig. 1. These planar sinks may represent ideal surfaces, grain boundaries, or interfaces. We define the PD concentration profile along the coordinate axis (z) perpendicular to the planar sinks. We assume that D_V and D_I do not depend on the spatial coordinates; i.e., they do not vary along the solute RIS profile. At steady state and along the z axis, the diffusion equations of SIAs and vacancies lead to the partial differential equations:

$$0 = \phi - K_R C_V C_I + D_V \frac{\partial^2 C_V}{\partial z^2}, \quad (28)$$

$$0 = \phi - K_R C_V C_I + D_I \frac{\partial^2 C_I}{\partial z^2}, \quad (29)$$

where $C_V(z)$ and $C_I(z)$ are respectively the local concentrations of vacancies and SIAs at coordinate z . At any position z , these local concentrations are related to each other by the

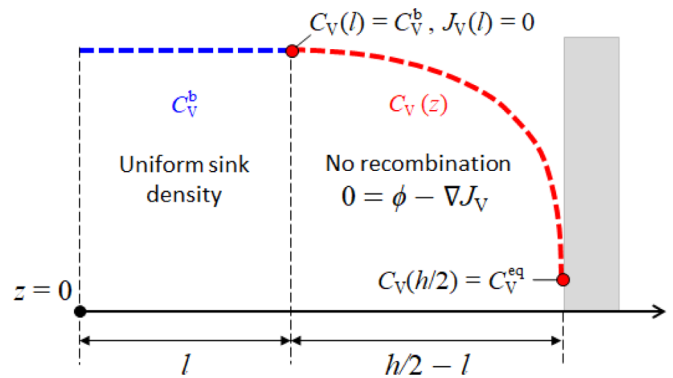


FIG. 1. Schema of vacancy concentration profile divided into two regions. In the first region ($0 < z < l$), the vacancy concentration is assumed to be uniform in space and given by a mean-field kinetic approach. In the second region ($l < z < h/2$), the PD recombination reactions are neglected and the vacancy concentration is given by $\nabla \cdot \mathbf{J}_V = \phi$.

steady-state relation $D_V[C_V(z) - C_V^{eq}] = D_I C_I(z)$, as demonstrated in Appendix D 1. Since C_V and C_I are related, in the following we consider only the spatial variation of C_V . Assuming that $D_I \gg D_V$, Eq. (28) is rewritten as follows:

$$\frac{\partial^2 C_V(z)}{\partial z^2} = -\frac{\phi}{D_V} + \frac{4\pi r_c}{\Omega} C_V(z) [C_V(z) - C_V^{eq}]. \quad (30)$$

This equation can be solved numerically, though it is CPU-time consuming and convergence might be difficult to reach when the nonlinear recombination reaction dominates. Finding an analytical solution would solve these issues. Besides, it would be a powerful tool for understanding how RIS varies with irradiation conditions and the microstructure (sink strength). However, for the time being, a general analytical solution of Eq. (30) does not exist [58–60]. Close to a planar sink and if we neglect the mutual recombination reactions between PDs (i.e., $r_c = 0$), there is a simple analytical solution of the PD concentration profile [28]. As explained in Ref. [28], the solution of Eq. (30) with $r_c = 0$ reads

$$C_V(z) = -a \left(z^2 - \frac{h^2}{4} \right) + C_V^{eq}, \quad (31)$$

where

$$a = \frac{\phi}{2D_V}, \quad (32)$$

h is the average spacing between planar sinks, and the position of the origin of axis ($z = 0$) is chosen to be at the midpoint between two planar sinks (see Fig. 1).

Close to a PD sink, ignoring the recombination reactions should be a reasonable hypothesis, because locally concentrations of PDs are very low. Hence their probability of recombination, that is proportional to the square of the PD concentrations, should be very low as well. Therefore, we split the PD concentration profiles in two regions: a bulk region far from sinks in which concentrations are uniform, and a sink region in which we account for the z variation of the PD concentration profile (cf. Fig. 1). The z coordinate of the bulk region ranges between 0 and l , whereas the z coordinate of the

sink region ranges from l to $h/2$, h being the distance between the planar sinks. In the bulk region, $C_V(z)$ is constant and equal to the steady-state bulk concentration C_V^b [see Eq. (16)]. From Eq. (31), we deduce the vacancy concentration profile $C_V(z)$, with $l \leq z \leq h/2$. In order to ensure the continuity of the vacancy concentration and its spatial derivative (i.e., the vacancy flux), we apply the boundary conditions

$$C_V(l^-) = C_V(l^+), \quad \frac{\partial C_V}{\partial z}(l^-) = \frac{\partial C_V}{\partial z}(l^+) = 0. \quad (33)$$

We assume that PD sinks are perfect sinks, meaning that the PD concentration at sinks is the equilibrium one (which depends on the local solute concentration at sinks):

$$C_V\left(\frac{h}{2}\right) = C_V^{\text{eq}}. \quad (34)$$

The solution is then given by

$$C_V(z) = \begin{cases} C_V^b, & 0 \leq z < l, \\ -a(z-l)^2 + C_V^b, & l \leq z \leq h/2, \end{cases} \quad (35)$$

where the characteristic distance l is defined as

$$l = \frac{h}{2} - \sqrt{\frac{C_V^{\text{exc}}}{a}}, \quad (36)$$

where $C_V^{\text{exc}} = C_V^b - C_V^{\text{eq}}$ corresponds to the vacancy excess concentration with respect to the equilibrium one. Note that the characteristic distance l depends on the interplanar distance h and C_V^{exc} . Both quantities are related to the microstructure. The interplanar distance h determines the sink strength of the parallel planar sinks [61]:

$$k_{\text{planar}}^2 = \frac{8}{h^2}. \quad (37)$$

Under the assumption that the sink strength of the system is determined by interfaces only, the overall sink strength $k^2 = k_{\text{planar}}^2$, and the planar sink strength fully determines C_V^b . Otherwise, if the microstructure contains several PD sinks, the bulk concentration of vacancies C_V^b should depend on the overall sink strength k^2 , with $k^2 > k_{\text{planar}}^2$. In this case, k^2 and h would be independent variables.

If $l < 0$, Eq. (35) is no longer appropriate, because the PD planar sinks are so close that it is not possible to introduce a bulk region with uniform concentrations. In this case, we set $l = 0$, and the obtained PD concentration profile is given by Eq. (31).

Using the Gibbs formalism of interface excess quantities, we define the vacancy concentration excess at sinks by the following integral:

$$S_V = \int_0^{h/2} [C_V(z) - C_V(0)] dz. \quad (38)$$

We obtain from Eq. (35) and Eq. (38) that

$$S_V = -\frac{(C_V^b - C_V^{\text{eq}})^{3/2}}{3\sqrt{a}}. \quad (39)$$

As expected, S_V is always negative. Note that the latter depends on the PD recombination reactions through the variation of C_V^b with R . Therefore, as stated in Sec. II B 1, we cannot ignore the recombination reactions, unless the recombination

rate (R) is negligible with respect to the PD elimination rate at sinks (K).

In the sink domain, i.e., $K \gg R$, we have

$$S_V = -\frac{\sqrt{2}}{3(k^2)^{3/2}} \left(\frac{\phi}{D_V} \right). \quad (40)$$

Therefore, S_V is proportional to the ratio ϕ/D_V , and it decreases with the sink strength k^2 .

In the recombination domain, i.e., $R \gg K$, we have

$$S_V = -\frac{1}{6} \left(\frac{\Omega}{\pi r_c} \right)^{3/4} \left(\frac{\phi}{D_V} \right)^{1/4}. \quad (41)$$

Thus, S_V is proportional to $(\phi/D_V)^{1/4}$, and it is independent of k^2 .

C. Radiation-induced segregation of solute atoms

From the vacancy RIS profile and the RIS factor expressed as functions of the local PD and solute concentrations, we derive an analytical expression of the solute RIS profile.

1. Local concentration-dependent RIS factor α

According to Wiedersich [12,13,30], at steady state, the concentration gradients of solutes and vacancies near an ideal sink are related by

$$\nabla C_B = -\alpha(z) \nabla C_V, \quad (42)$$

with the RIS factor

$$\alpha(z) = \frac{d_{AI} d_{AV} C_A C_B}{d_{AI} D_B C_A + d_{BI} D_A C_B} \alpha_s \quad (43)$$

and

$$\alpha_s = \frac{d_{BI}}{d_{AI}} - \frac{d_{BV}}{d_{AV}}. \quad (44)$$

α_s determines the sign of the RIS factor α , which in turn determines the sign of RIS. In a dilute binary alloy A(B), the partial diffusion coefficients d_{BI} , d_{AI} are systematically positive, while d_{AV} is systematically negative. On the other hand, d_{BV} is either positive or negative. The off-diagonal coefficient L_{BV} determines the sign of d_{BV} . Concerning the sign of α_s , we consider two cases. When d_{BV} is positive, i.e., vacancies drag solute atoms, α_s is positive and RIS leads to solute enrichment around sinks. When d_{BV} is negative, the sign of α_s depends on the relative amplitude of the partial diffusion coefficient ratios d_{BI}/d_{AI} and d_{BV}/d_{AV} . Note that a steady-state gradient of solute concentration can only be established if a backward diffusion opposes the solute gradient resulting from flux coupling. The rate of this backward reaction is governed by the intrinsic diffusion coefficients D_A and D_B that appear in the denominator of $\alpha(z)$.

The local RIS factor α depends on the z coordinate through the variation of the local concentration C_B and C_V with z [see Eq. (43)]. In order to analyze the variation of α with the local concentrations of vacancies and solute atoms, we rewrite α by making explicit its variation with C_B and C_V . Note that we neglect PD concentration with respect to the solute and solvent concentration, i.e., $C_A = 1 - C_B$. We deduce from

Eqs. (12), (17), and (43) that

$$\alpha(z) = \frac{\alpha_1 C_B(z)}{C_V(z) + \alpha_2}, \quad (45)$$

where

$$\alpha_1 = \frac{\alpha_0}{\alpha_V + \alpha_1}, \quad (46)$$

$$\alpha_2 = \frac{\alpha_{\text{mono}} - \alpha_1 C_V^{\text{eq}}}{\alpha_V + \alpha_1}, \quad (47)$$

with

$$\begin{aligned} \alpha_0 &= \alpha_s C_A d_{AI} d_{AV}, \\ \alpha_V &= C_A d_{AI} d_{BV}^c + C_B d_{BI} d_{AV}^c, \\ \alpha_1 &= (C_A d_{AI} d_{BI}^c + C_B d_{BI} d_{AI}^c) D_V / D_I, \\ \alpha_{\text{mono}} &= (C_A d_{AI} + C_B d_{BI}) L_{BB}^{\text{mono}}. \end{aligned}$$

Therefore, α decreases with C_V . The RIS factors α_1 and α_2 are independent of the PD concentrations. Instead, they vary with C_B because the partial diffusion coefficients d_{ij} depend on C_B . However, along a RIS profile, the relative variation of the solute concentration is a lot smaller than that of the PD concentration. Hence, we assume that α_1 and α_2 do not vary along the RIS profile, and we compute these coefficients at C_B equal to the nominal solute concentration. This assumption is later justified by a comparison between the solute RIS profile obtained from our analytical approximation and the exact solution (cf. Fig. 18).

2. Steady-state RIS profile of solute atoms

Following Eq. (35), we deduce the vacancy concentration gradient ∇C_V . Then, from Eqs. (42) and (45), we obtain the solute concentration gradient

$$\frac{\nabla C_B}{C_B}(z) = \begin{cases} 0, & 0 \leq z < l, \\ -\frac{2\alpha_1(z-l)}{(z-l)^2 - b^2}, & l \leq z \leq h/2, \end{cases} \quad (48)$$

with $b^2 = (C_V^b + \alpha_2)/a$.

We determine α_1 and α_2 from the nominal solute concentration, \bar{C}_B . We derive the concentration profile of the solute atoms by integrating Eq. (48) with respect to z . We deduce the constants of integration from the following boundary conditions:

$$C_B(l^-) = C_B(l^+), \quad (49)$$

$$\int_0^{h/2} C_B(z) dz = \frac{h}{2} \bar{C}_B. \quad (50)$$

These conditions ensure the continuity of the solute concentration profile C_B at $z = l$ and the mass conservation of the solute atoms along the RIS profile.

Note that in this study we neglect the equilibrium segregation of solutes resulting from the interaction of solutes with the sink [62–64]. This thermodynamic property may strongly modify the solute concentration over the first two or three atomic planes of the sink [62,63]. Its amplitude and width (generally less than 1 nm) vary with the temperature, the chemical nature of solute atoms, and the nature of the sink. A quantitative investigation of this phenomenon would require

a detailed knowledge of the structure of the sink as well as the solute segregation energies at different atomic sites near the sink. Even in the case of a positive and high equilibrium solute segregation, the volume fraction of segregated lattice sites is so small that it should not much affect the bulk solute concentration, unless this concentration is very small. If the equilibrium segregation is so strong that a large number of solute atoms are found at interfaces, there would be fewer solute atoms left in the bulk to interact with PDs and participate in RIS. This could be reproduced effectively by lowering the value of the nominal solute concentration parameter used in our model. Note that equilibrium segregation as well as RIS is diminished by a FAR mechanism. Therefore, in the case of a relatively weak equilibrium segregation, the kinetics of the solute RIS, as well as the average width of the RIS profiles (spreading over a few tens of nanometers [2]), should not be much affected.

According to the boundary conditions, i.e., Eqs. (49) and (50), we obtain

$$C_B(z) = \begin{cases} K_1 b^{-2\alpha_1}, & 0 \leq z < l, \\ K_1 [b^2 - (z-l)^2]^{-\alpha_1}, & l \leq z \leq h/2, \end{cases} \quad (51)$$

with

$$K_1 = \frac{h}{2} \frac{\bar{C}_B}{l b^{-2\alpha_1} + \int_0^{(h/2)-l} (b^2 - z^2)^{-\alpha_1} dz}. \quad (52)$$

Note that there is no simple analytical expression of the integral $I = \int_0^{(h/2)-l} (b^2 - z^2)^{-\alpha_1} dz$. Nevertheless, we can calculate it from the hypergeometric function ${}_2F_1$ [65] (presented in Appendix D 2).

Similarly to Eq. (39), we define the total amount of solute atoms segregated at sinks as the solute concentration excess $S_B = (h/2)[\bar{C}_B - C_B(0)]$. This is written

$$S_B = \frac{h}{2} (\bar{C}_B - K_1 b^{-2\alpha_1}). \quad (53)$$

In cases where we cannot ignore the FAR mechanism, the diffusion of isolated solute atoms (L_{BB}^{mono}) and thus α_2 are not negligible. α_2 increases with the FAR frequency, which in turn decreases the RIS of solute atoms. In the extreme case where $\alpha_2 \gg C_V^b$, we obtain, for $0 < z < (h/2) - l$,

$$z^2 < \left(\frac{h}{2} - l\right)^2 < C_V^b/a \ll b^2. \quad (54)$$

In this case, $I \simeq [(h/2) - l] b^{-2\alpha_1}$, $K_1 = \bar{C}_B b^{2\alpha_1}$, and the amount of segregated solute is zero ($S_B = 0$).

On the contrary, if we ignore FAR, $\alpha_2 \ll C_V^b$. If we also neglect C_V^{eq} , $b = (h/2) - l$ and we obtain

$$\begin{aligned} I &= \int_0^b (b^2 - z^2)^{-\alpha_1} dz \\ &= b^{-2\alpha_1+1} I_{\alpha_1}, \end{aligned} \quad (55)$$

with

$$I_{\alpha_1} = \int_0^1 (1 - z^2)^{-\alpha_1} dz. \quad (56)$$

Note that I_{α_1} is positive and only depends on the RIS factor α_1 . Moreover, it is larger than 1 if the solute RIS is positive (i.e.,

$\alpha_1 > 0$), and smaller than 1 in the opposite case. Then, after Eqs. (52), (53), and (55), we may approximate S_B as follows:

$$S_B = \frac{h}{2} \bar{C}_B \frac{I_{\alpha_1} - 1}{I_{\alpha_1} + \frac{l}{(h/2)^{-l}}} \quad (57)$$

$$= \frac{h}{2} \bar{C}_B \frac{I_{\alpha_1} - 1}{I_{\alpha_1} - 1 + \frac{h}{2} \sqrt{\frac{a}{C_V^b}}}. \quad (58)$$

According to Eq. (57), S_B is positive if the solute RIS factor is positive, and negative otherwise.

Besides, following Eqs. (39) and (58), we obtain a direct relationship between S_B and S_V :

$$S_B = \frac{h}{2} \bar{C}_B \frac{I_{\alpha_1} - 1}{I_{\alpha_1} - 1 - \frac{h}{2} \frac{C_V^b}{S_V}}. \quad (59)$$

We observe that the amount of solute RIS, S_B , is directly related to α_1 and S_V/C_V^b . In the denominator, C_V^b is the signature of the backward diffusion opposing the RIS solute concentration gradient. This backward diffusion is the reason why solute RIS (S_B), unlike PD RIS (S_V), is not systematically governed by the ratio ϕ/D_V .

In the sink domain ($K \gg R$), we obtain from Eq. (22) and Eq. (58) that

$$S_B = \frac{h}{2} \bar{C}_B \frac{I_{\alpha_1} - 1}{I_{\alpha_1} - 1 + \frac{h}{2} \sqrt{\frac{k^2}{2}}}. \quad (60)$$

In this case, S_B is independent of the ratio ϕ/D_V , whereas it decreases with k^2 , as already shown in Ref. [28]. Thus, at fixed k^2 , if we neglect the small variation of α_1 with the dose rate ϕ , the solute RIS amount is independent of ϕ [28]. Besides, S_B varies with temperature through the variation of α_1 with temperature. Note that the present expression of S_B is not exactly the same as the one published in Ref. [28], because here we do not assume that the RIS factor is independent of solute and PD concentrations.

In the recombination domain ($K \ll R$), we obtain from Eq. (23) and Eq. (58) that

$$S_B = \frac{h}{2} \bar{C}_B \frac{I_{\alpha_1} - 1}{I_{\alpha_1} - 1 + \frac{h}{2} \left(\frac{\Omega}{\pi r_c}\right)^{-1/4} \left(\frac{\phi}{D_V}\right)^{1/4}}. \quad (61)$$

S_B is then governed by the ratio ϕ/D_V as well as by the RIS factor α_1 . Moreover, it decreases with the dose rate ϕ .

D. Interplay between RIS and the microstructure

According to the analytical derivation, the RIS segregation profiles between parallel planar sinks depend upon the spacing h between the parallel planar sinks, and the total sink strength $k^2 = \sum_s k_s^2$ of the overall microstructure including the local parallel planar sink strength [Eq. (37)]. Such a modeling of the PD sink population allows for the investigation of the RIS profile of a local sink interacting with the overall microstructure. Note that our analytical model of RIS could be easily extended to other local sinks, such as dislocation lines k_{line}^2 and dislocation loops k_{loop}^2 .

In the following, for the sake of simplicity, we consider parallel sink planes as the major PD sinks. This means that we ignore the contributions of other types of sinks, and relate the interplanar distance to the total sink strength: $h = \sqrt{8/k^2}$.

TABLE I. *Ab initio* solute-PD binding energies (in eV) of Fe alloys obtained in Ref. [27] for mixed B-I dumbbell configuration, and Ref. [47] for 1-NN and 2-NN B-V pair configurations. Negative energies stand for attractive interactions.

Configuration	Fe-P	Fe-Mn	Fe-Cr	Fe-Si	Fe-Ni	Fe-Cu
Mixed B-I	-1.03	-0.56	-0.05	+0.00	+0.19	+0.38
1-NN B-V	-0.38	-0.17	-0.06	-0.30	-0.10	-0.26
2-NN B-V	-0.27	-0.11	-0.01	-0.11	-0.21	-0.17

III. RESULTS

We apply the above RIS models to the specific case of Fe-based dilute alloys. We start this section with a brief presentation of these alloys from a perspective of their PD energy properties. Then we present a parametric study of the variation of steady-state vacancy concentration with temperature, radiation flux, and sink strength, with the aid of 2-D maps. We extend this parametric approach to the solute diffusion coefficients, the flux-coupling and RIS factors, and the vacancy and solute RIS profiles. Note that in the temperature-radiation flux maps, the recombination radius r_c is set to $\sqrt{3}a_0$, and the sink strength is set to $k^2 = 5 \times 10^{14} \text{ m}^{-2}$ (i.e., $h = 126 \text{ nm}$), unless otherwise specified.

A. DFT energy database of dilute Fe-based alloys

The vacancy formation enthalpy H_V^f and entropy S_V^f in pure iron are respectively set to 2.18 eV and $4.1k_B$, and the lattice parameter a_0 to 2.831 Å according to previous DFT calculations [27]. The *ab initio* solute-PD binding energies, migration energies, and jump frequency prefactors are found in Ref. [27] for the vacancy diffusion mechanism, and in Ref. [47] for the dumbbell diffusion mechanism.

The computation of the RIS factors in these alloys has shown that the general flux-coupling behavior is largely governed by the short-range thermodynamic interaction between PDs and solute atoms [27]. The range of vacancy-solute pair interactions is considered up to 6-NN, while the range of SIA-solute pair interactions is up to 5-NN. We list in Table I the binding energy values of the mixed dumbbell and the 1- and 2-NN solute-vacancy pairs. In the six binary alloys, the 1- and 2-NN solute-vacancy binding energies are negative; i.e., the solute atoms are attracted by the vacancy. Moreover, Cr has a very weak interaction with vacancies compared with the other solute atoms. Concerning the SIAs, the most stable configuration is the dumbbell one. Based on the binding energies of the solute-Fe mixed dumbbells, we can divide the Fe-based dilute alloys into two groups: those with stable (P, Mn, Cr) and nonstable (Si, Ni, Cu) mixed dumbbells.

Note that the kinetic behaviors of the solute atoms forming nonstable mixed dumbbells (Si, Ni, Cu) should be predominantly controlled by the vacancy mechanism [47]. In addition, the values of the 1-NN and 2-NN solute-vacancy binding energies in Fe-Si, Fe-Ni, and Fe-Cu alloys are close. Therefore, the kinetic properties of the solute atoms are expected to be similar in these alloys. On the other hand, for the group of solutes forming stable mixed dumbbells (P, Mn, Cr), the values of solute-PD binding energies cover a wider range,

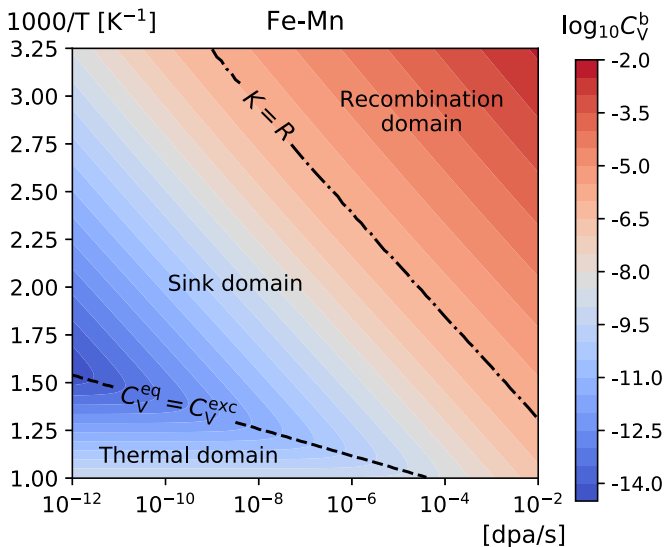


FIG. 2. Bulk vacancy concentration C_V^b as a function of dose rate (in dpa) and inverse temperature (in K^{-1}) for the dilute Fe-Mn alloy. The nominal solute concentration \bar{C}_{Mn} is set to 1 at. % and the sink strength k^2 is set to $5 \times 10^{14} m^{-2}$. The main trends of C_V^b with T and ϕ are similar for the other investigated Fe alloys.

suggesting that the kinetic properties can be very different in Fe-P, Fe-Mn, and Fe-Cr alloys.

B. Bulk vacancy concentration at steady state

As shown in Sec. II C, the RIS of solute atoms is related to the bulk vacancy concentration. Thus, the kinetic domains of solute RIS are similar to the PD kinetic domains. Therefore,

we compute the steady-state bulk concentration of vacancies with respect to temperature, radiation flux, and sink strength.

First, we compute the variation of the bulk vacancy concentration, C_V^b , with temperature (T) and dose rate (ϕ). In Fig. 2, the result for the Fe-Mn system is represented in the form of a ϕ - T map, in which the colors indicate the amplitude of C_V^b . This map can be divided into three domains: thermal domain when the bulk vacancy concentration is lower than twice the equilibrium vacancy concentration, i.e., the effect of irradiation is negligible; sink domain for $K > R$; recombination domain for $R > K$.

According to Eqs. (22) and (23), C_V^b decreases with T , whereas it increases with ϕ . In the recombination domain, C_V^b increases linearly with ϕ . In both the recombination and sink domains, each level line corresponds to a fixed value of ϕ/D_V . In the thermal domain, the level lines are horizontal because C_V^b is close to the equilibrium vacancy concentration C_V^{eq} , and independent of ϕ .

We find that the main trends of C_V^b with T and ϕ are similar for the other investigated Fe alloys (not presented), with only slight variations of the extent of the kinetic domains. Therefore, we conclude that the solute effect on the bulk concentration of vacancies is negligible.

C. Solute diffusion

We compute the intrinsic solute diffusion coefficient, D_B , which is equivalent in a dilute alloy to the solute tracer diffusion coefficient. The ϕ - T maps of D_B are presented in Fig. 3. For the six alloys, we recover the three kinetic domains of C_V^b . Over most irradiation conditions of interest, $C_B \gg C_V^b$ (see Fig. 2). In this case, the solute diffusion coefficient varies

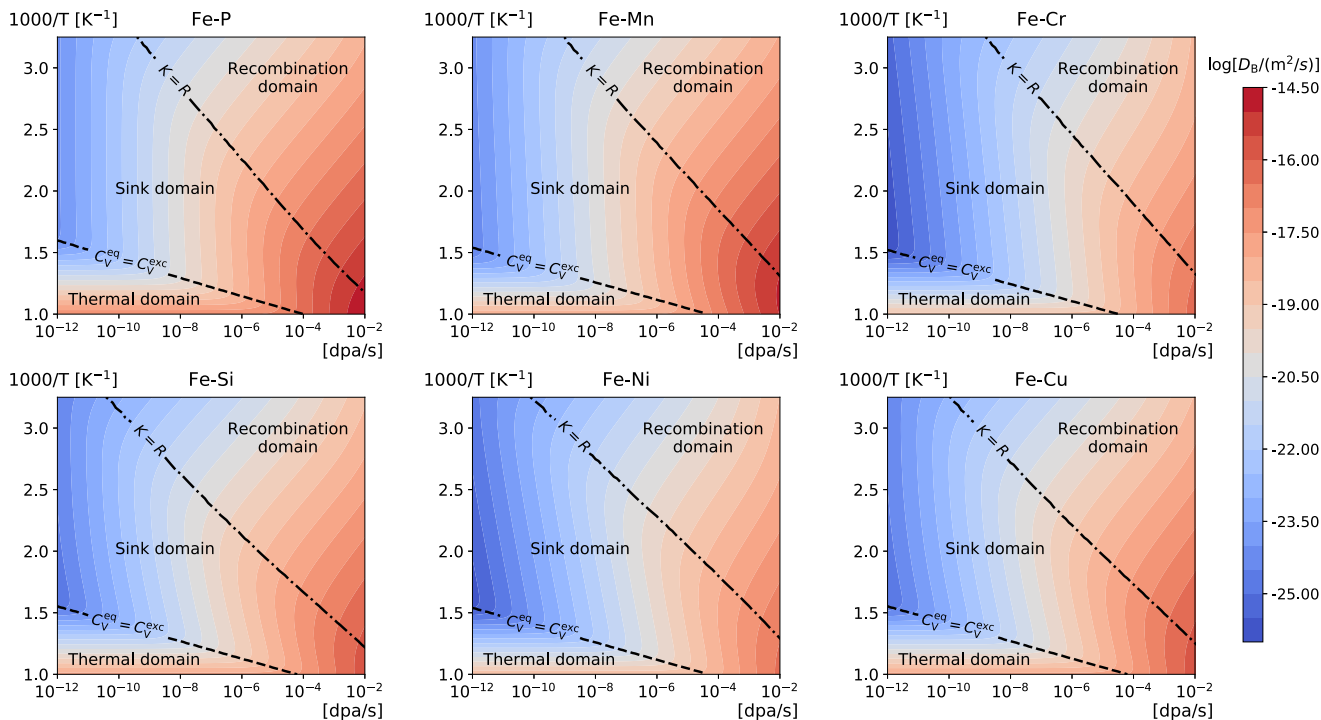


FIG. 3. Solute diffusion coefficient D_B as a function of dose rate (in dpa) and inverse temperature (in K^{-1}) for several dilute binary Fe-based alloys. The nominal solute concentration \bar{C}_B is set to 1 at. % and the sink strength k^2 is set to $5 \times 10^{14} m^{-2}$.

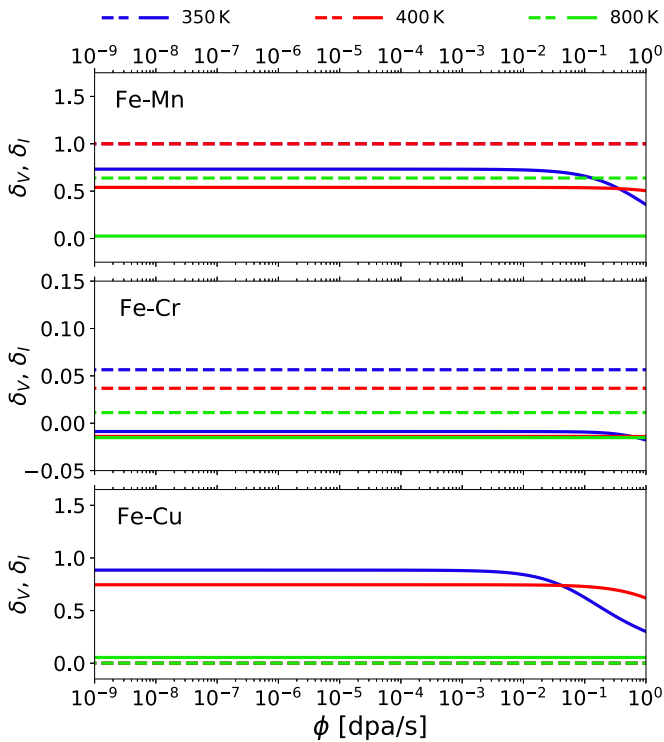


FIG. 4. Flux-coupling coefficients for Fe-Mn, Fe-Cr, and Fe-Cu alloys, mediated by vacancies (solid lines) and SIAs (dashed line), as functions of dose rate. The results are obtained for three different temperatures: 350 K, 450 K, and 800 K. The nominal solute concentration \bar{C}_B is set to 1 at. % and the sink strength k^2 is set to $5 \times 10^{14} \text{ m}^{-2}$.

linearly with the bulk vacancy concentration [cf. Eq. (11)], provided the effect of FAR is negligible. Therefore, we expect the same kinetic domains, except in the low-temperature and high-flux domain where FAR may affect the solute diffusion properties and \bar{C}_B has the same order of magnitude as C_V^b .

D_B increases with temperature in the recombination and thermal domains, though the increasing rate is different in the two domains. In the sink domain, D_B is nearly T -independent. As for the effect of the radiation flux, D_B increases with ϕ except in the thermal domain. Similarly to C_V^b , the solute effect on the main trends is weak.

D. Flux coupling

1. Flux-coupling coefficients

As expected from the solute-PD binding energy database (Table I), the overall RIS of solute atoms in Fe-Si, Fe-Ni, and Fe-Cu alloys is mainly due to flux coupling mediated by the vacancy diffusion mechanism, whereas in Fe-P, Fe-Mn, and Fe-Cr alloys both the dumbbell and vacancy mechanisms contribute to the solute RIS [47]. In addition, in Fe-Cr alloy, flux couplings mediated by vacancies and SIAs have opposite sign, and the subsequent sign and amplitude of Cr RIS results from a temperature-dependent balance between the vacancy-induced depletion and the dumbbell-induced enrichment.

In Fig. 4, we plot the variation of the flux-coupling coefficients with dose rate in Fe-Mn, Fe-Cr, and Fe-Cu alloys at different temperatures. For $\phi < 10^{-2} \text{ dpa/s}$, we observe that

in the Fe-Cu alloy, δ_I is much smaller than δ_V because of the instability of the mixed solute-dumbbell configuration. We observe similar trends in Fe-Si and Fe-Ni alloys. For Fe-Mn, Fe-P, and Fe-Cr alloys, both δ_I and δ_V have a non-negligible contribution. The above results are consistent with the flux-coupling behaviors presented in Ref. [47], even though the FAR mechanism was therein not included. In Ref. [6], we have shown that there is an effect of FAR whenever the jump frequencies of PDs at equilibrium are comparable with FAR frequencies within 1 to 2 orders of magnitude. Therefore, as expected, we observe an effect of FAR on δ_V at significant dose rates ($> 10^{-2} \text{ dpa/s}$) and low temperatures ($< 400 \text{ K}$), a flux-temperature domain in which the FAR frequency is close to or higher than thermal jump frequencies. Note that at temperatures above 350 K, the flux-coupling coefficient δ_I is nearly independent of dose rate below 1 dpa. This is because the dumbbell-mediated jump frequencies are much higher than the FAR frequency.

2. RIS factor α_1

The RIS factor results from the balance between flux coupling and backward diffusion opposing the segregation of solute atoms at sinks. Here, we consider the RIS factor α_1 , which, in the absence of FAR, corresponds to the overall RIS factor [cf. Eq. (46)]. In Fig. 5, we show the temperature-radiation flux maps of α_1 . As expected from the solute-PD binding energies (E_b), α_1 has the same behavior in Fe-Si, Fe-Ni, and Fe-Cu alloys. When $\phi < 10^{-2} \text{ dpa/s}$, the absolute value of α_1 decreases with temperature because of the drop of the vacancy-solute pair probability proportional to $\exp(-E_b/k_B T)$ [27]. In the Fe-P, Fe-Mn, and Fe-Cr systems, the variation of α_1 with temperature is quite different. In Fe-P, the absolute value of α_1 increases with temperature. As for the Fe-Mn alloy, $|\alpha_1|$ increases up to around 650 K. The binding energy of the Fe-Mn dumbbell is lower than that of the Fe-P dumbbell. As a consequence, above 650 K, $|\alpha_1|$ decreases with temperature. Regarding the Fe-Cr alloy, we observe a change of sign of α_1 around 530 K.

At low temperatures, roughly below 600 K, α_1 decreases with radiation flux. At temperatures below 300 K and under very high radiation fluxes (above $\phi = 1 \text{ dpa/s}$), α_1 is close to 0 because flux coupling is totally destroyed by FAR. Above 600 K and/or below 10^{-2} dpa/s , there is no effect of FAR on α_1 . Note that even though FAR may reduce the magnitude of α_1 , it does not qualitatively change the extent of the three kinetic domains, or the sign of the RIS factor.

3. RIS factor α_2

In addition to α_1 , the RIS magnitude depends also on the RIS factor α_2 , which is directly related to the FAR mechanism (i.e., L_{BB}^{mono}). As stated in Sec. II C 1, the ratio

$$\gamma = \alpha_2 / C_V^b \quad (62)$$

indicates the extent of the FAR effect on the solute RIS. If $\gamma \gg 1$, S_B is equal to 0. In Fig. 6, we plot the ϕ - T maps of $|\gamma| = |\alpha_2| / C_V^b$. Dashed lines represent level lines of γ . We observe that over most flux-temperature conditions, γ is smaller than 0.1. It is close to or larger than 1 at high ϕ and low

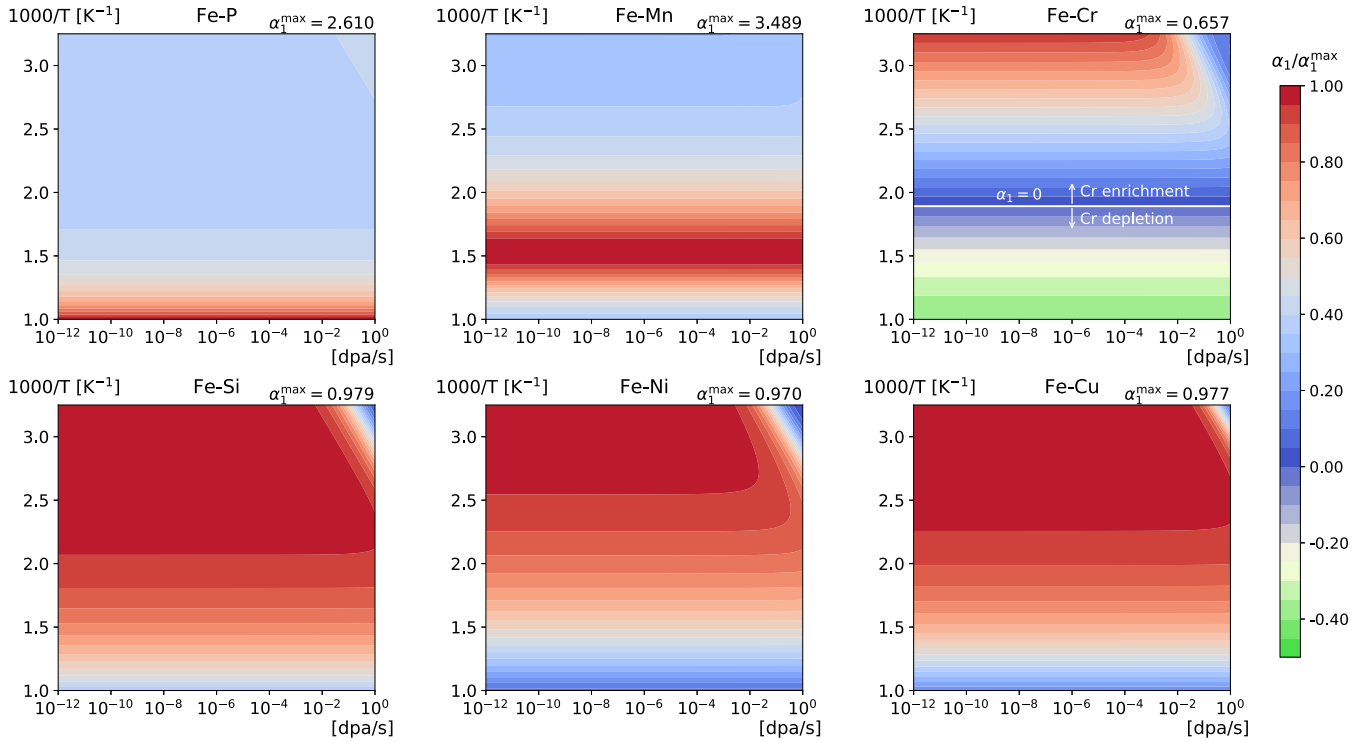


FIG. 5. RIS factor α_1 normalized by its maximum value α_1^{\max} as a function of dose rate (in dpa) and inverse temperature (in K⁻¹) in several dilute binary Fe-based alloys. The solid line in Fe-Cr system corresponds to $\alpha_1 = 0$. The nominal solute concentration \bar{C}_B is set to 1 at. % and the sink strength k^2 is set to $5 \times 10^{14} \text{ m}^{-2}$.

T , and increases with dose rate. Furthermore, it decreases with temperature, and becomes negative above a threshold tem-

perature linearly increasing with radiation flux. The domain where $\gamma < 0$ coincides with the thermal domain of Fig. 2. At

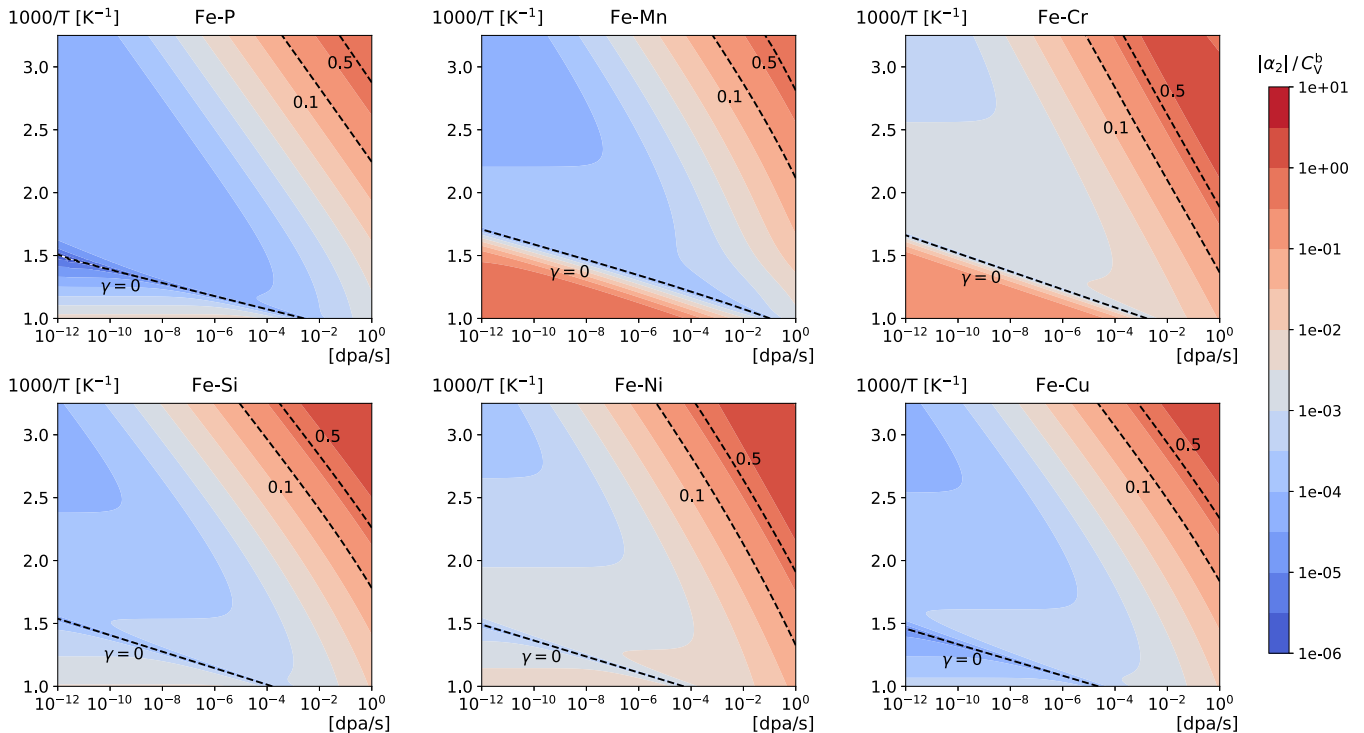


FIG. 6. $|\gamma| = |\alpha_2|/C_V^b$ as a function of dose rate (in dpa) and inverse temperature (in K⁻¹) in several dilute binary Fe-based alloys. The nominal solute concentration \bar{C}_B is set to 1 at. % and the sink strength k^2 is set to $5 \times 10^{14} \text{ m}^{-2}$.

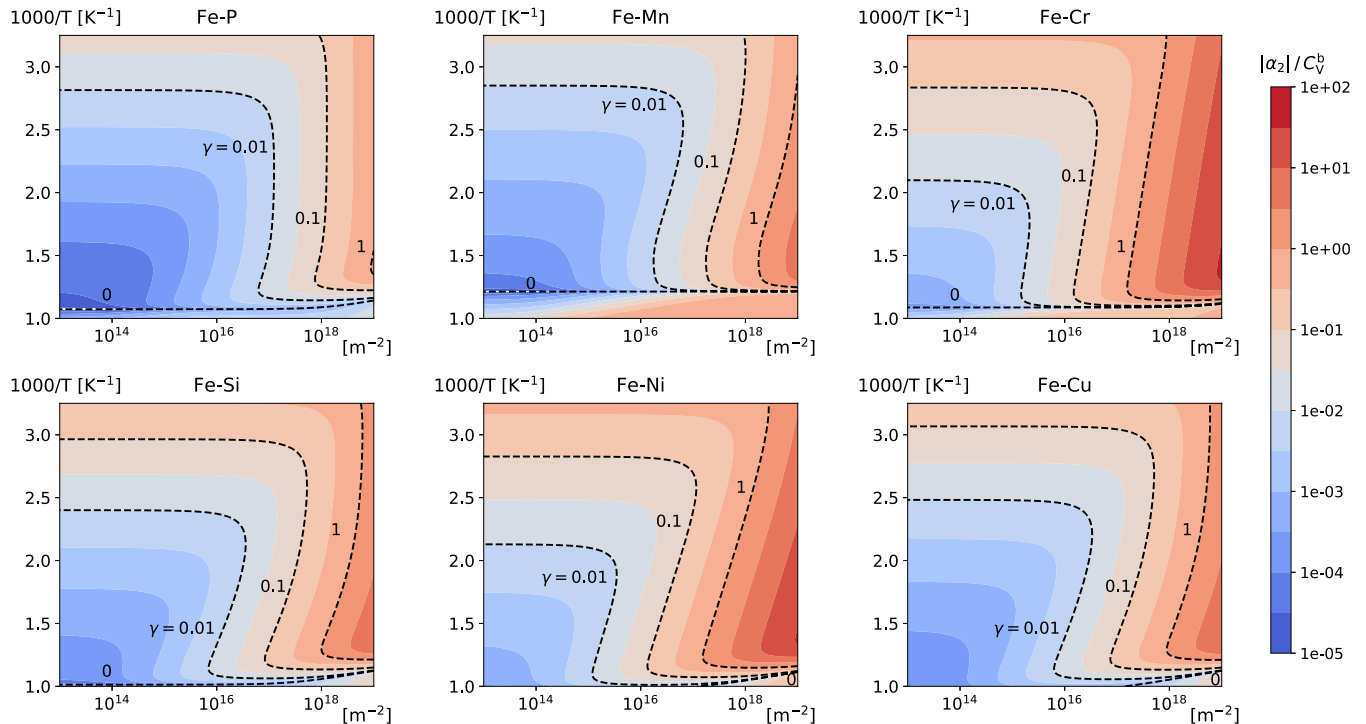


FIG. 7. $|\gamma| = |\alpha_2|/C_V^b$ as a function of sink strength (in m^{-2}) and inverse temperature (in K^{-1}) in several dilute binary Fe-based alloys. The nominal solute concentration \bar{C}_B is set to 1 at. % and ϕ is set to 2×10^{-4} dpa/s.

the limit of this domain, C_V^b is close to the equilibrium vacancy concentration C_V^{eq} .

In order to highlight the effect of sink strength on γ , we plot the k^2 - T maps of $|\gamma|$ in Fig. 7. Since γ increases with k^2 , the FAR effect on RIS should be significant at large values of k^2 .

Note that the variation of γ with T , ϕ , and k^2 is alloy-specific. For a given set of parameters, the value of γ is relatively high in Fe-Ni and Fe-Cr, small in Fe-P and Fe-Mn, and in an intermediate range in Fe-Si and Fe-Cu alloys.

E. Radiation-induced segregation of PDs

In order to investigate the effect of PD recombination on the RIS profiles, we compare the profiles given by two different methods: (i) the analytical approximation proposed in this work [Eq. (35) for $C_V(z)$], and (ii) the one proposed in Ref. [28] where the recombination rate is set to zero.

The concentration profiles of vacancies at different temperatures and sink strengths are plotted in Fig. 8. In order to assess the accuracy of the analytical approximations, we plot as well the reference profile obtained from the exact solution of Eq. (30) computed by a finite-difference method. We observe that the concentration profiles obtained from the present analytical approach are in good agreement with the reference profiles.

When recombination reactions are neglected, the vacancy concentration along the RIS profile is overestimated, especially at low temperatures (e.g., 600 K) and small sink strength (e.g., $5 \times 10^{13} \text{ m}^{-2}$), because the ratio K/R is relatively large. Therefore, the recombination effect is not negligible (see Sec. II B 2). In order to investigate the shape of the vacancy

RIS profile at different irradiation conditions, we define an effective width l_V^e of the vacancy concentration profile as

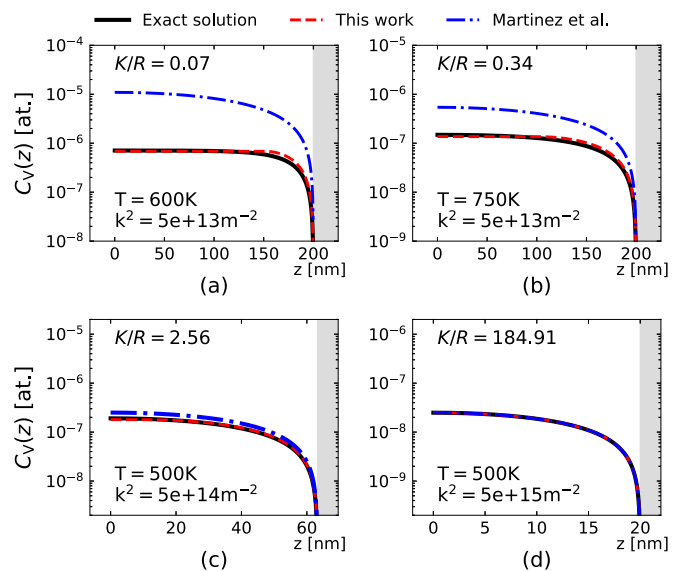


FIG. 8. Concentration profiles of vacancies under irradiation. The solid lines are the exact solutions of Eq. (30). The dashed and dash-dotted lines are the analytical approximations of Eq. (30), obtained from Eq. (35) (this work) and Eq. (31) (cf. Ref. [28]), respectively. The shaded area indicates the sink. The results for (a) and (b) are respectively given for $T = 600 \text{ K}$ and 750 K , with $\phi = 10^{-4}$ dpa/s and $k^2 = 5 \times 10^{13} \text{ m}^{-2}$ (i.e., $h = 400 \text{ nm}$). The results for (c) and (d) are respectively given for $k^2 = 5 \times 10^{14} \text{ m}^{-2}$ and $5 \times 10^{15} \text{ m}^{-2}$, with $\phi = 10^{-6}$ dpa/s and $T = 500 \text{ K}$.

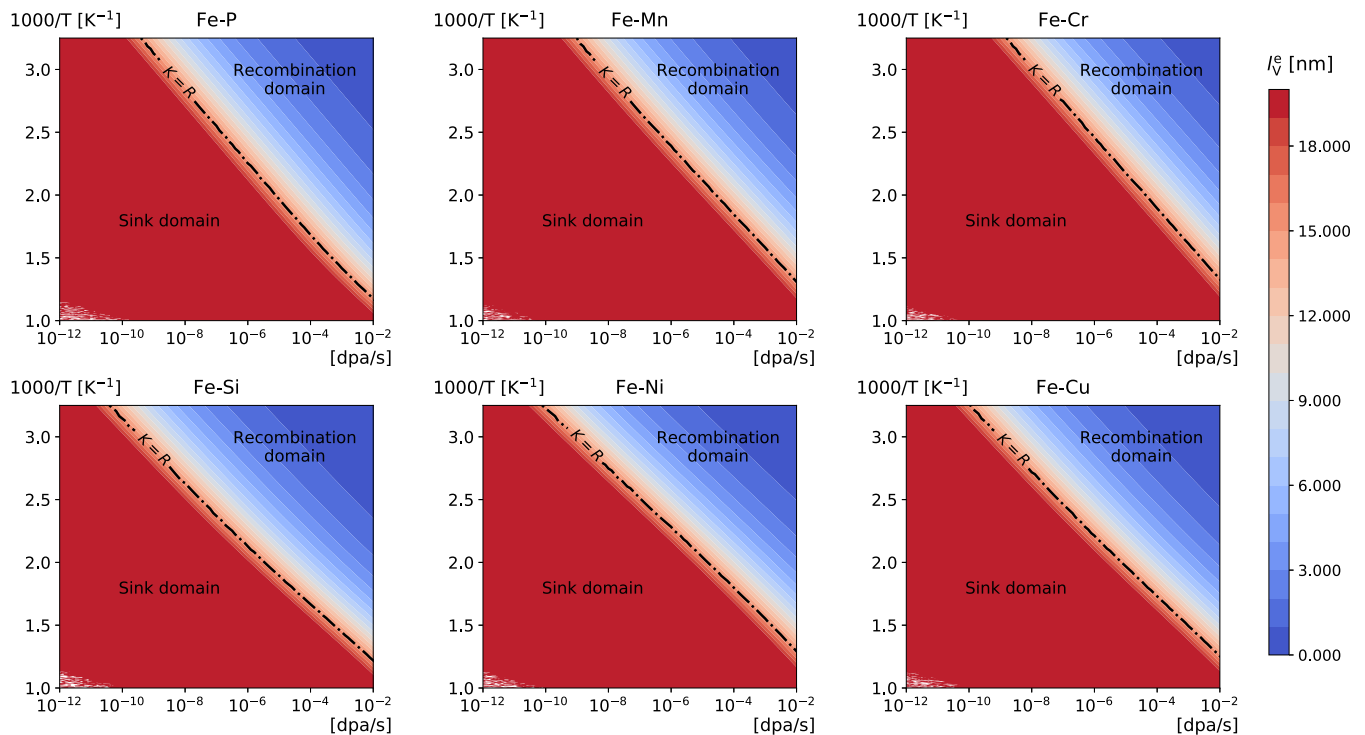


FIG. 9. The effective width of RIS profiles of vacancies as a function of dose rate (in dpa) and inverse temperature (in K^{-1}) for several dilute binary Fe-based alloys. The nominal solute concentration \bar{C}_B is set to 1 at. % and the sink strength k^2 is set to $5 \times 10^{14} m^{-2}$. The corresponding distance between planar sinks is $h = 126$ nm.

follows:

$$l_V^e = \sqrt{\frac{\int_0^{h/2} [(h/2) - z]^2 [C_V(z) - C_V(0)] dz}{\int_0^{h/2} [C_V(z) - C_V(0)] dz}} \quad (63)$$

$$= \frac{1}{\sqrt{10}} \left(\frac{h}{2} - l \right). \quad (64)$$

This parameter represents the average distance between a vacancy and a PD sink. It is also related to the width of the vacancy-depleted zone near sinks [66]. In Fig. 9, we plot the maps of l_V^e as a function of the inverse temperature and dose rate. In the sink domain, $l \rightarrow 0$ and therefore the width of the vacancy profile equals $h/\sqrt{40}$, whatever the irradiation conditions. According to Eq. (64), l_V^e increases with h . Therefore, the smaller the sink density, the larger the distance between sinks, and the wider the vacancy-depleted zone. In the recombination domain, l_V^e decreases with dose rate, while it increases with temperature.

Furthermore, we investigate the effect of temperature, dose rate, and sink strength on the segregation amount of vacancies. Note that, using Eq. (40) and Eq. (41), $\log_{10} |S_V|$ is given by

$$\log_{10} |S_V| = \begin{cases} \log_{10} \phi - \log_{10} D_V - \frac{3}{2} \log_{10} k^2 + K_2, & K \gg R, \\ \frac{1}{4} \log_{10} \phi - \frac{1}{4} \log_{10} D_V + K_3, & K \ll R, \end{cases} \quad (65)$$

with $K_2 = \log_{10}(\sqrt{2}/3)$ and $K_3 = \log_{10}[(\Omega/\pi r_c)^{3/4}/6]$.

Figure 10 shows the maps of $\log_{10} |S_V|$ near the interface [given by Eq. (39)] as a function of inverse temperature and dose rate. The maps are divided into two domains correspond-

ing to the two limit cases of Eq. (65). The first kinetic domain is the one dominated by recombination reactions ($K < R$), and the second one is the sink domain ($K > R$). In both regimes, $\log_{10} |S_V|$ increases linearly with $\log_{10} \phi$ and $1/T$, but the slopes are different.

Figure 11 shows the temperature-sink strength maps of the same quantity, divided as well into recombination and sink domains. $\log_{10} |S_V|$ decreases linearly with $\log_{10} k^2$ in the sink domain, whereas it is nearly k^2 -independent in the recombination domain. The variations of S_V with ϕ and k^2 are similar in all investigated Fe-based binary alloys, whereas the variations with $1/T$ are a bit more varied because the average vacancy diffusion coefficient D_V is alloy-specific.

F. Radiation-induced segregation of solute atoms

As done for the vacancy concentration profile, we introduce an effective width of the concentration profile of solute atoms (l_B^e) to characterize the shape of the solute RIS profile. Its definition is similar to that of the vacancies [Eq. (64)], where subscript V is replaced by B. Figure 12 shows the ϕ - T maps of l_B^e . This quantity is large and almost uniform in the thermal domain. In the recombination domain, l_B^e decreases with dose rate and increases with temperature. These trends are very similar to the ones observed for l_V^e . As a result, we expect the RIS profiles of vacancies and solute atoms to have almost the same width in thermal and recombination domains. In these domains, we could rely on the measured width of the solute RIS profiles to obtain information on the vacancy RIS profile, and subsequently on the PDs sink strength. On the other hand, in the sink domain, the larger the solute RIS amount, S_B , the smaller the width of the RIS profile, l_B^e .

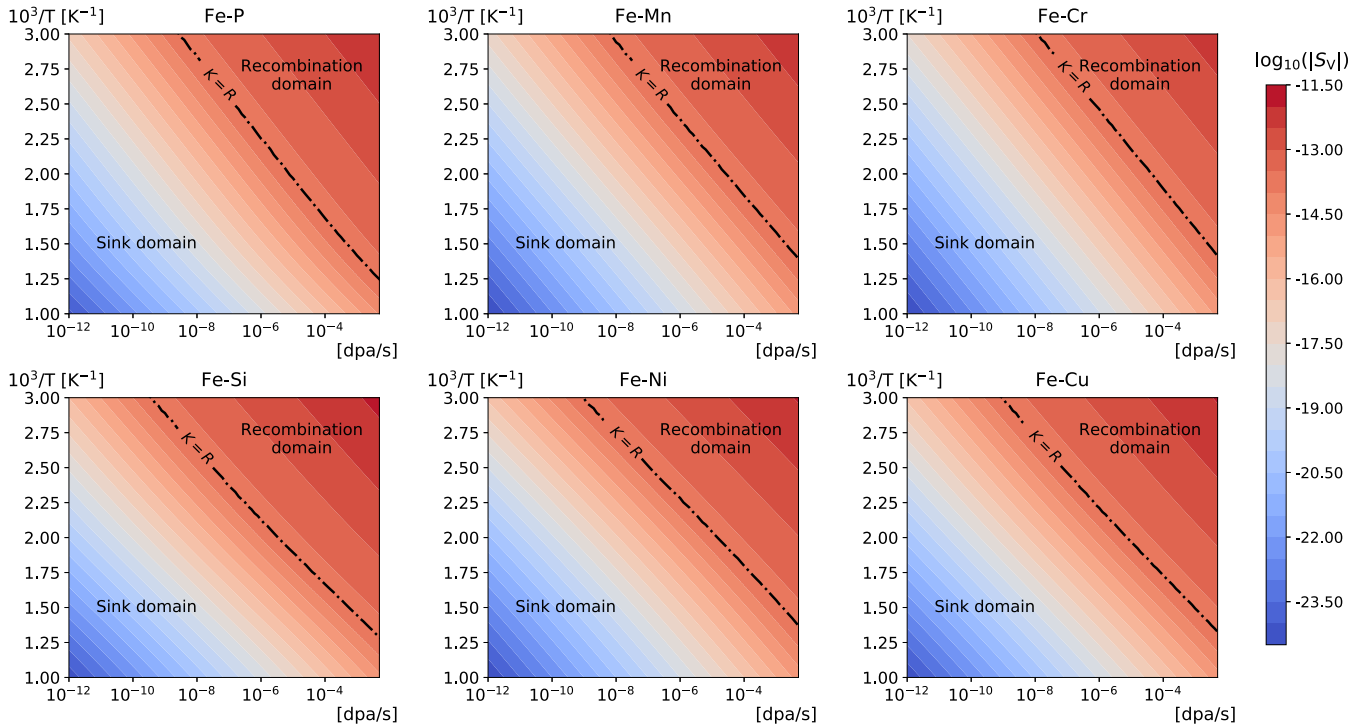


FIG. 10. Total amount of segregated vacancies S_V as a function of dose rate (in dpa) and inverse temperature (in K^{-1}) for several dilute binary Fe-based alloys. The nominal solute concentration \bar{C}_B is set to 1 at. % and the sink strength k^2 is set to $5 \times 10^{14} m^{-2}$.

Moreover, I_B^e is smaller than I_V^e in this domain, especially in Fe-P and Fe-Mn alloys where the tendency to positive RIS is significant.

Furthermore, Figs. 13 and 14 show the temperature-radiation flux-sink strength maps of the solute RIS amount given by Eq. (53). As shown in Fig. 3, the flux-temperature

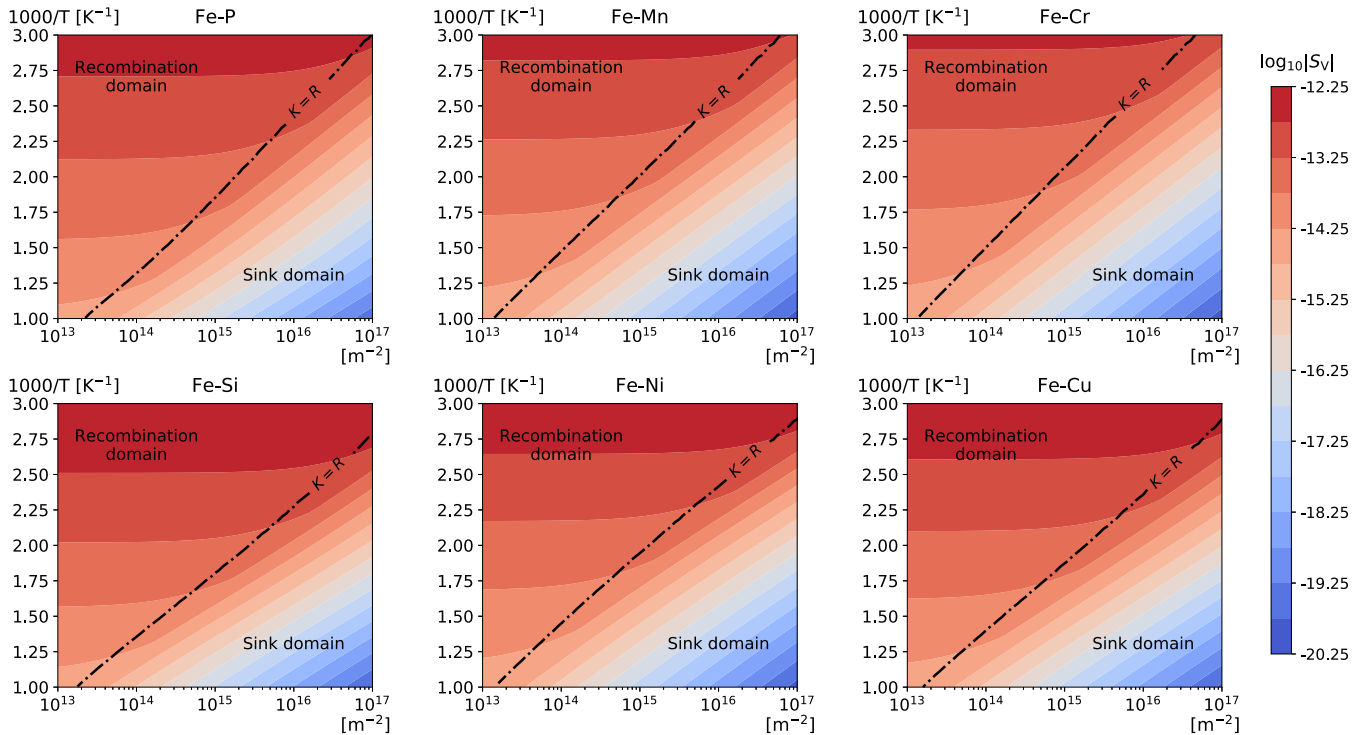


FIG. 11. Total amount of segregated vacancies S_V as a function of sink strength (in m^{-2}) and inverse temperature (in K^{-1}) for several dilute binary Fe-based alloys. The nominal solute concentration \bar{C}_B is set to 1 at. % and the dose rate ϕ is set to 2×10^{-4} dpa/s.

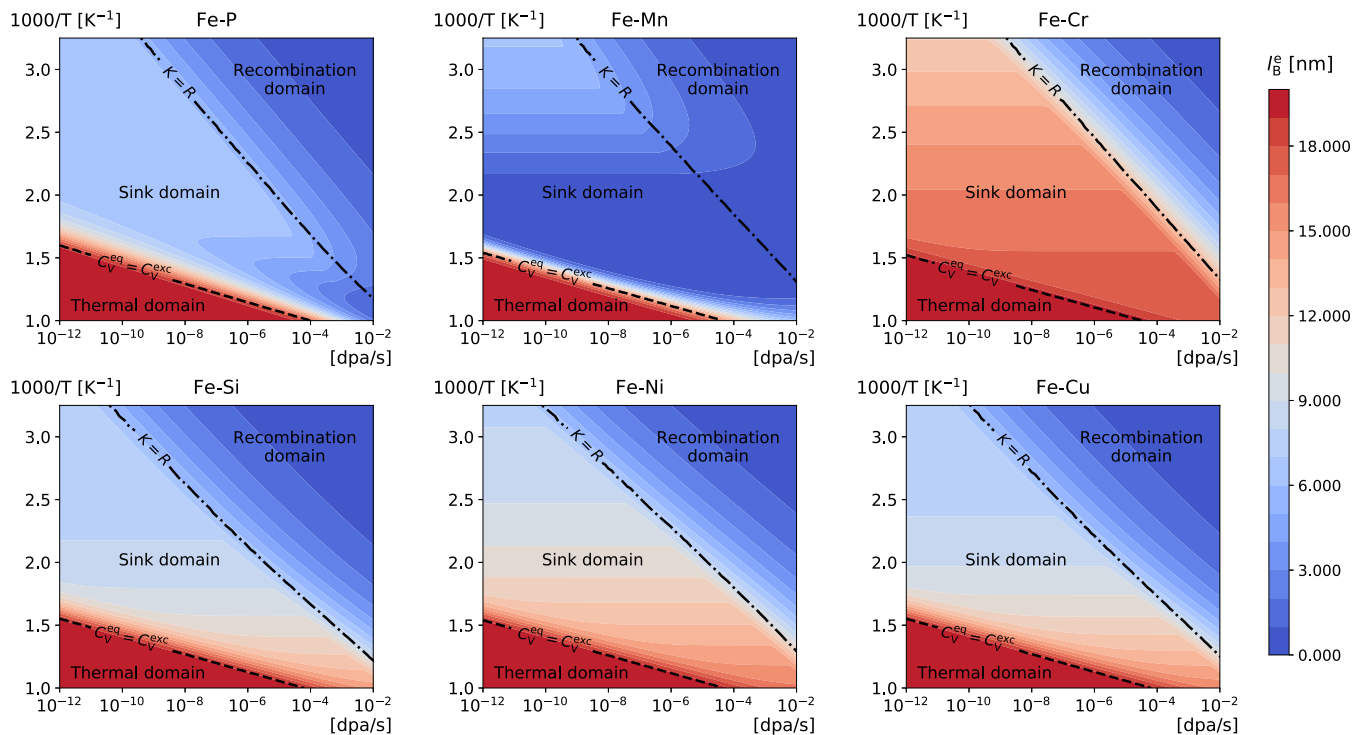


FIG. 12. The effective width of RIS profiles of solute atoms as a function of dose rate (in dpa) and inverse temperature (in K^{-1}) for several dilute binary Fe-based alloys. The nominal solute concentration \bar{C}_B is set to 1 at. % and the sink strength k^2 is set to $5 \times 10^{14} m^{-2}$. The corresponding distance between planar sinks is $h = 126$ nm.

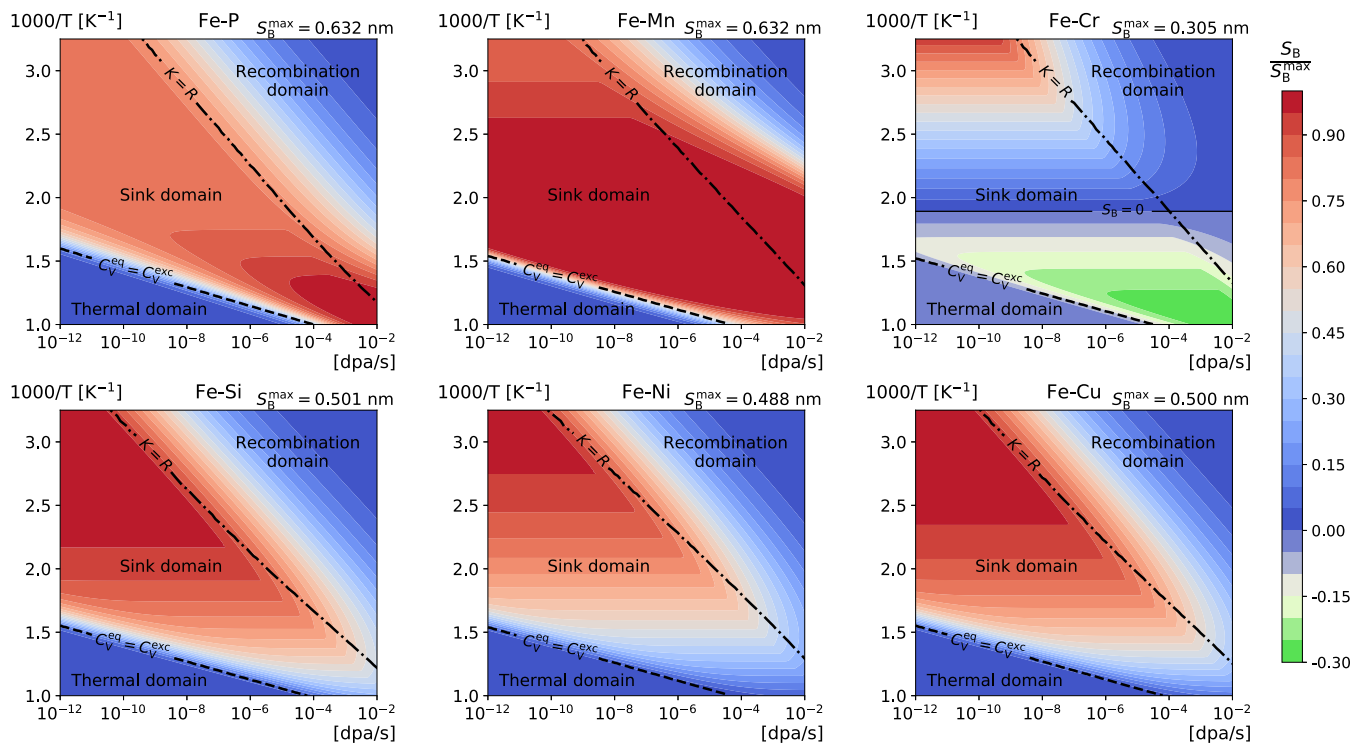


FIG. 13. Total amount of segregated solute atoms S_B normalized by its maximum over all considered irradiation conditions S_B^{max} as a function of dose rate (in dpa) and inverse temperature (in K^{-1}) for several dilute binary Fe-based alloys. The nominal solute concentration \bar{C}_B is set to 1 at. % and the sink strength k^2 is set to $5 \times 10^{14} m^{-2}$.

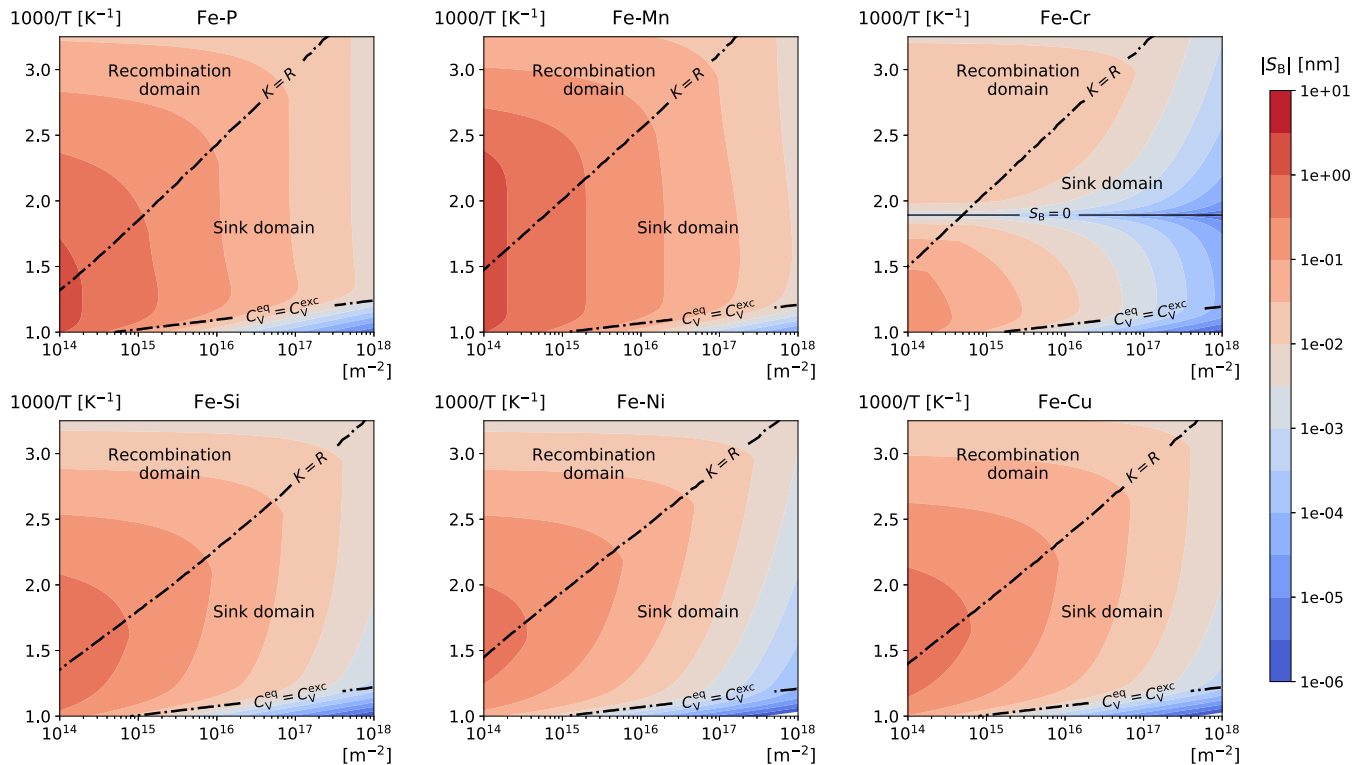


FIG. 14. Total amount of segregated solute atoms S_B as a function of sink strength (in m^{-2}) and inverse temperature (in K^{-1}) for several dilute binary Fe-based alloys. The nominal solute concentration \bar{C}_B is set to 1 at. % and the dose rate $\phi = 2 \times 10^{-4}$ dpa/s.

(ϕ - T) domains of S_B are mainly determined by PD kinetics. S_B is significant in the sink domain, whereas it is relatively small in the recombination domain because, after the SIA-V recombination, only a few PDs are left for the long-distance solute diffusion toward the sinks. In the thermal domain, since the amount of excess PDs is very small, so is the net flux of PDs toward sinks, which leads to small S_V and S_B .

In Fig. 13, we show the maps of the solute RIS amount S_B as a function of T and ϕ at fixed sink strength $k^2 = 5 \times 10^{14} \text{ m}^{-2}$. As expected, S_B does not depend on dose rate in the sink domain [cf. Eq. (60)], and S_B decreases with dose rate in the recombination domain [cf. Eq. (61)]. In Fig. 14, we show the maps of S_B as a function of k^2 and T at fixed radiation flux $\phi = 2 \times 10^{-4}$ dpa/s. In the domain of PD elimination ($K > R$), S_B decreases with k^2 , as expected from Eq. (60).

We take the Fe-Cr alloy as an example to illustrate the effect of sink strength on the extent of the kinetic domains and the maximum of solute RIS. Figure 15 shows the Cr RIS amount maps at different sink strength k^2 . Note that the sink domain grows wider with increasing k^2 . However, the maximum RIS amount, $S_{\text{Cr}}^{\text{max}}$, decreases with sink strength. Therefore, an increase of sink concentration or strength decreases the solute RIS at each sink. We obtain the same trends for the other Fe-based alloys (not represented).

The variation of S_B with T , ϕ , and k^2 strongly depends on the chemical nature of solute atoms because α_1 and α_2 are alloy-specific (see Fig. 5 and Fig. 6). As expected from the DFT-based data of the solute-PD binding energies (I), the main trends are similar in Fe-Si, Fe-Ni, and Fe-Cu alloys,

but very different in Fe-P, Fe-Mn, and Fe-Cr alloys. In Fe-Si, Fe-Ni, and Fe-Cu alloys, the highest solute enrichment tendency is at low temperatures (about 400 K) and dose rate (about 10^{-12} dpa/s), whereas the highest solute enrichment tendency in Fe-P is at high temperatures (> 1000 K) and dose rates (around 10^{-3} dpa/s). As for Mn solutes, the peak of RIS occurs at intermediate temperatures (about 650 K) and dose rate (from 10^{-10} to 10^{-6} dpa/s). For Cr solutes, the peak of positive RIS occurs at low temperatures (about 300 K) and dose rates (about 10^{-11} dpa/s), whereas the peak of negative RIS occurs at high temperatures (> 800 K) and dose rates ($> 10^{-6}$ dpa/s).

As stated in Sec. III D 3, the FAR effect on the solute RIS should be significant at large k^2 because, in this case, γ is close to or larger than 1. We take the Fe-Ni alloy as an example to investigate the FAR effect on the solute RIS profile. In order to identify the FAR effect, we calculate and compare the C_{Ni} profiles and segregation amounts S_{Ni} at different FAR intensities, which are characterized by the values of n_{FAR} (i.e., the number of FAR per dpa). Note that $n_{\text{FAR}} = 0$ indicates that there is no FAR in the displacement cascade. The concentration profiles are plotted in Figs. 16(a) and 16(b) with two different sink strengths and n_{FAR} equal to 0, 50, 100, and 500. At $k^2 = 5 \times 10^{14} \text{ m}^{-2}$, the segregation profiles are practically insensitive to FAR effects, because $\gamma < 0.01$ and FAR can be neglected. However, at $k^2 = 10^{16} \text{ m}^{-2}$, the RIS profiles strongly depend on the FAR intensity n_{FAR} . The concentration of solute atoms at the interface decreases with n_{FAR} . Moreover, the amount of segregated Ni atoms also decreases with n_{FAR} [Fig. 16(c)]. At $k^2 = 10^{16} \text{ m}^{-2}$ and $n_{\text{FAR}} = 500$, S_{Ni} is less than about half the one without FAR (i.e., $n_{\text{FAR}} = 0$) at

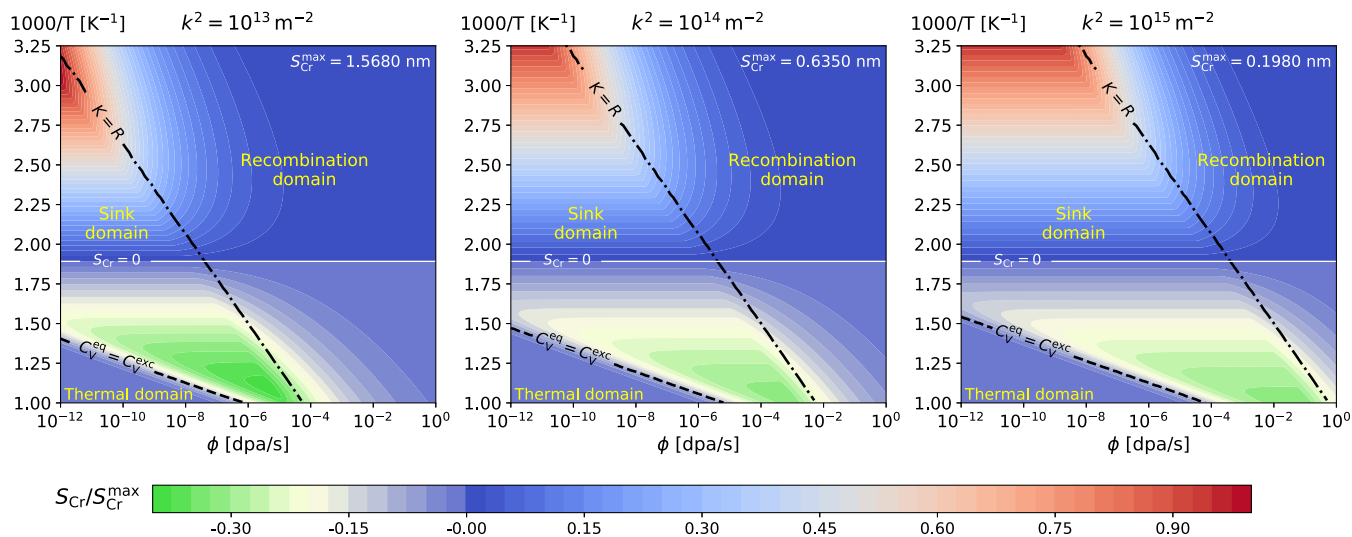


FIG. 15. Total amount of segregated Cr atoms S_{Cr} as a function of dose rate (in dpa) and inverse temperature (in K^{-1}) computed for different sink strengths: $10^{13} m^{-2}$, $10^{14} m^{-2}$, and $10^{15} m^{-2}$. The results are normalized by the maximum segregation amount S_{Cr}^{max} . The nominal solute concentration \bar{C}_B is set to 1 at. %.

both investigated temperatures (600 and 750 K). We observe similar tendencies in the other five Fe-based dilute alloys. This FAR effect is significant close to the interface. In this region, the vacancy concentration is low, and the thermally activated backward diffusion of solutes is limited. In this case, FAR is the major mechanism for backward diffusion. Therefore, RIS models ignoring FAR events overestimate the RIS tendencies in Fe-based alloys, especially at large sink strengths. In order to help identify at which dose rate the effect of FAR on RIS is non-negligible, we define a critical dose rate beyond which the relative difference between the segregation amounts obtained with and without FAR effect is larger than 25%. In Table II, we provide the orders of magnitude of the critical dose rates at different sink strengths, temperatures, and irradiation particles. Around reactor temperature (500–600 K), heavy ions are much more likely to induce FAR effects than electrons and protons at a realistic dose rate.

IV. DISCUSSION

A. Dose rate compensation by a temperature shift

One objective of this work is to provide quantitative temperature-shift criteria for ion-irradiation experiments aimed at emulating RIS generated by neutron irradiation. We ascribe the difference of structural evolution between neutron and ion irradiations to a difference of radiation flux. A change of temperature may compensate the effect of a change of the radiation flux on the vacancy profile or on the solute RIS. With this work, we can suggest temperature shifts that should be applied depending on the (evolving) microstructure and the RIS quantity that one wants to reproduce (S_V or S_B). Even though S_B and S_V are interdependent quantities [cf. Eq. (59)], the behavior of solute RIS is very different from that of PDs, mainly because solute RIS results from a balance between the solute flux triggered by a PD driving force and the backward solute flux triggered by a solute concentration gradient, whereas such

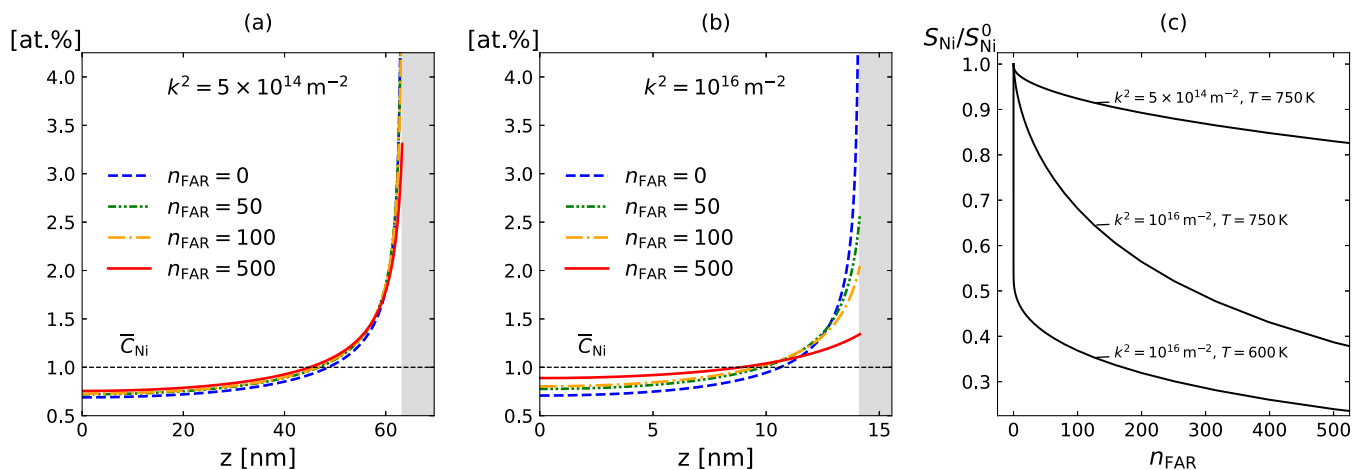


FIG. 16. Ni segregation profile $C_{Ni}(z)$ near an interface (indicated by the shaded area) computed for (a) $k^2 = 5 \times 10^{14} m^{-2}$ and $T = 750 K$; (b) $k^2 = 10^{16} m^{-2}$ and $T = 750 K$; and (c) Ni segregation amount with different FAR intensities at $T = 600$ and $700 K$. S_{Ni}^0 is the segregation amount obtained with $n_{FAR} = 0$. The nominal solute concentration \bar{C}_{Ni} is set to 1 at. % and the dose rate ϕ is set to 10^{-4} dpa/s.

TABLE II. Critical dose rates beyond which the relative difference between the segregation amounts obtained with and without FAR effect is larger than 25%, estimated at various temperatures, sink strengths, and incident particles.

T (K)	k^2 (m^{-2})	Critical dose rate (dpa/s)		
		Electrons ($n_{\text{FAR}} \simeq 1$)	Protons ($n_{\text{FAR}} \simeq 10$)	Heavy ions ($n_{\text{FAR}} \simeq 100$)
500	$10^{14}, 10^{15}$	~ 1	$\sim 10^{-2}$	$\sim 10^{-3}$
	10^{16}	~ 1	$\sim 10^{-2}$	$\sim 10^{-9}$
600	$10^{14}, 10^{15}$	> 1	~ 1	$\sim 10^{-2}$
	10^{16}	> 1	~ 1	$\sim 10^{-8}$

backward flux does not occur for PDs. Another difficulty is that the behavior of both PDs and solutes depends not only on the radiation flux and temperature, but also on the evolving microstructure sink strength. The latter is a complex function of temperature, radiation dose rate, and radiation dose (i.e., dose rate \times time), as shown in Fig. 17. Besides, the evolution of S_V and S_B as a function of sink strength, radiation flux, and temperature differs from one kinetic domain to another, and the extent of each kinetic domain in terms of temperature and radiation flux depends itself on the sink strength which evolves over time. Note that if the kinetic domains differ between neutron and ion irradiations, it is almost impossible to provide a temperature shift procedure. Nevertheless, there are a few limiting cases (defined in Table III) which provide some insights in this rather complex interplay and from which some quantitative temperature-shift criteria can be proposed.

In case (i), the sink strength is assumed to be constant during irradiation. A typical example is a material with an

initial metallurgical state including a high dislocation density, for instance a cold-worked material. In such material, stable dislocation networks are formed and the microstructure does not evolve under irradiation. The corresponding sink strength should be high, such that the system is in the sink domain. At fixed sink strength, the amount of vacancy RIS, S_V , increases linearly with the ratio ϕ/D_V in the sink domain. On the other hand, S_B is independent of ϕ in the sink domain. Thus, if the vacancy RIS is to be conserved from a neutron to a higher flux ion irradiation, we prescribe a shift of temperature such as to keep the ratio ϕ/D_V constant. Concerning the RIS of PDs, we recover the Mansur's invariant relation, which has been established in the recombination domain for swelling phenomena [42]. However, for the solute RIS in the sink domain, there is no need for a change of temperature to keep the amount of solute RIS constant.

In case (ii), irradiation conditions are such that both the neutron and ion irradiated alloys remain in the recombination domain. This happens when the sink density is initially low and the radiation dose rate is weak enough not to disturb the microstructure too much. In this case, our results suggest that S_V and S_B are nearly independent of k^2 (cf. Figs. 11 and 14). S_V increases with $(\phi/D_V)^{1/4}$ in the recombination domain, while S_B decreases with ϕ/D_V . Note that a temperature shift conserving the ratio ϕ/D_V does not necessarily ensure a correct emulation of a neutron radiation-induced solute RIS. Therefore, one temperature shift only enables us to reproduce one RIS quantity, either the PD segregation profile or the solute RIS. Indeed, the solute-PDs flux couplings leading to solute RIS are strongly nonlinear and alloy-specific functions of temperature. Nevertheless, we may use our temperature-flux maps to obtain an estimation of the temperature shift leading to the same amount of solute RIS. According to the maps of Fig. 10 and Fig. 13, an emulation of neutron irradiation with a flux of 10^{-7} dpa/s at $T = 360$ K (i.e., $1000/T = 2.75$) by means of an ion irradiation of 10^{-5} dpa/s would require a shift of temperature $\Delta T \simeq +90$ K for the PDs, and alloy-dependent ΔT for solute RIS as listed in Table IV. Note that no temperature shift is proposed for Fe-Cr alloy because S_{Cr} at $\phi = 10^{-5}$ dpa/s, at any temperature, is systematically smaller than that at $\phi = 10^{-7}$ dpa/s and $T = 360$ K.

In case (iii), the alloys irradiated by neutrons and ions remain in the sink domain. This is often the case with alloys irradiated at high dose, in which a large number of sinks (e.g., dislocation loops, voids) are formed. We may assume that the temperature shift is sufficiently small such that the variation of α_1 can be neglected. Thus, S_B only depends on the microstructure [cf. Eq. (60)]. We assume that the timescale for the establishment of solute RIS is shorter than the characteristic

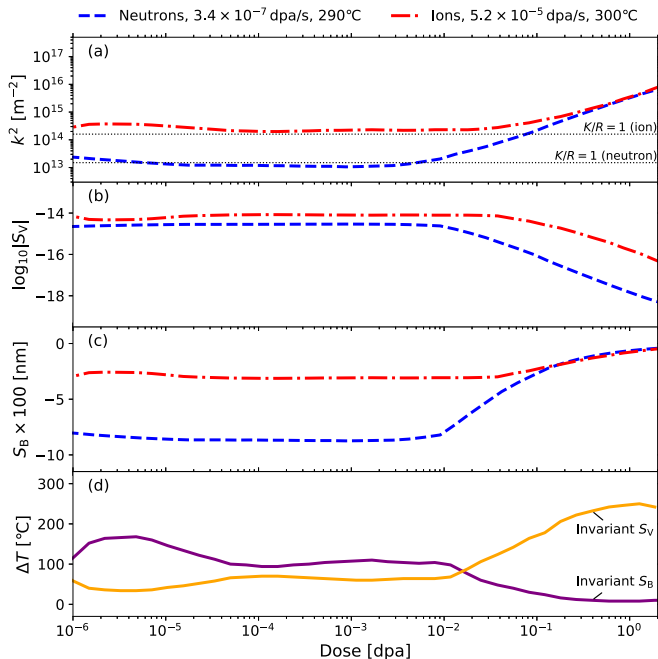


FIG. 17. The evolution of (a) the sink strength k^2 , (b) the amount of vacancy RIS S_V , and (c) the amount of solute RIS S_B in the Fe-Cr alloy irradiated by neutrons and ions. The evolution of the temperature shift for ion irradiation that is required to emulate the neutron RIS is plotted in (d). The plots of k^2 are reproduced from the results in Ref. [68]. The dotted guiding lines obtained from $K/R = 1$ are plotted in (a) to help identify the kinetic domain.

TABLE III. Definition of cases in which quantitative criteria of temperature shift ΔT can be proposed.

Cases	Assumptions	Criteria for S_V	Criteria for S_B
(i)	$K \gg R$ and k^2 independent of ϕ and T (e.g., a cold-worked material with a high sink density)	Invariant ϕ/D_V	No temperature shift is needed ($\Delta T = 0$)
(ii)	$K < R^a$ (e.g., a material with an initial low sink density, irradiated at a low dose such that the sink strength remains small)	Invariant ϕ/D_V	Invariant $\frac{I_{\alpha_1-1}}{I_{\alpha_1-1+\frac{h}{2}(\frac{\Omega}{\pi r_c})^{-1/4}(\frac{\phi}{D_V})^{1/4}}}$
(iii)	$K > R^a$ (e.g., a material subjected to a high dose of irradiation leading to the formation of a microstructure with a high sink strength)	Invariant $\frac{1}{(k^2)^{3/2}}(\frac{\phi}{D_V})$	(a) If ΔT is sufficiently small such that the variation of α_1 is negligible (e.g., within about ± 50 K from Fig. 5): invariant k^2 (b) Else: invariant $\frac{h}{2} \frac{I_{\alpha_1-1}}{I_{\alpha_1-1+\frac{h}{2}\sqrt{k^2}}}$
(iv)	$k^2(\phi, T)$ is given	We use our models to calculate S_V and S_B with k^2 varying with ϕ and T . We search for at which temperature (T_2) the ion irradiation at $\phi = \phi_2$ reproduces the same S_V or S_B obtained from the neutron irradiation at $T = T_1$ and $\phi = \phi_1$ (e.g., Fig. 17).	

^aConditions for both neutron and ion irradiations. One can refer to Fig. 15 to help identify the kinetic domains at different irradiation conditions and sink strengths.

time of the evolving microstructure, because as soon as there is a flux of PDs toward sinks, a gradient of PD and solute concentrations is formed. The solute concentration profile reaches its stationary shape during the time it takes for the solute backward diffusion to reach its stationary regime, which is fast since it requires diffusion over the nanoscale distance of a RIS profile compared to the evolution of the microstructure which requires long-range diffusion of PDs. Hence, we expect that solute RIS adiabatically follows the microstructural evolution. Based on this assumption, the temperature-shift criterion for S_B is the one ensuring an invariant sink strength. Therefore, given the variations of k^2 with temperature and dose rate, the variations of S_B should have the same trends. This is consistent with the experimental observation in Ref. [35]. In this experiment, the authors attempted to emulate the microstructure of a cold-worked 316-stainless steel produced by a neutron irradiation at 320 °C by a self-ion irradiation at higher temperatures. In such cold-worked material, the sink density was relatively high; thereby the irradiation must take place in the sink domain. The authors in this study observed that self-ion irradiation at 380 °C produces dislocation loop size and density which matched well with those obtained with neutron irradiation. In the same study, they showed that the RIS behaviors from these two irradiation conditions coincided as well. Therefore, this experiment shows that a relatively small temperature shift ($+60$ °C in this experiment) ensuring an invariant microstructure (i.e., sink strength) is able to

reproduce as well the RIS behaviors for materials irradiated in the sink domain.

In case (iv), we assume that the evolution of the sink strength is not affected by the RIS of solutes. In this case, there are simulation methods and/or experimental studies yielding the evolution of the PD microstructure with respect to the irradiation conditions and the radiation dose [67,68]. The authors in Ref. [68] simulated the microstructural evolution of a Fe-Cr alloy irradiated by neutrons (3.4×10^{-7} dpa/s) and ions (5.2×10^{-5} dpa/s) at similar temperatures using cluster dynamics and atomic kinetic Monte Carlo simulations. Relying on their results, we can predict the evolution of the RIS behaviors. Note that their results indicate that the PD clusters are the major sinks. Due to the lack of information on cluster densities, we estimate the average distance between sinks directly from the sink strength by Eq. (37). In Fig. 17, we plot k^2 (from Ref. [68]) and S_V and S_B (from our calculation) as a function of the radiation dose. The evolution of k^2 indicates that, up to 0.01 dpa for neutron irradiation and 0.1 dpa for ion irradiation, the system is at the frontier between the recombination and sink domains. After these doses, the system is in the sink domain and the sink strengths of both neutron and ion irradiation conditions are close to each other. The calculated S_B in the two irradiation conditions are as well very similar after 0.1 dpa. This is because, in the sink domain, S_B depends only on α_1 and k^2 [as presented in case (iii)]; since the temperatures are close in the two irradiation conditions, the calculated S_B is nearly the same whenever the sink strengths are very close to each other. Below 0.01 dpa, both S_V and S_B in the two irradiation conditions are different. Given the variation trends of the sink strength with the irradiation conditions, we propose a temperature shift that would reproduce either the same S_V or the same S_B as in neutron irradiation from an ion irradiation experiment. As a qualitative approach, we assume that the sink strength k^2 is proportional to S_V . This approach should be reasonable because PD clusters are major sinks and their growth should be proportional to the PD segregation amount. Thus, by assuming

TABLE IV. Temperature shift required to simulate the solute RIS from the neutron irradiation with a flux of 10^{-7} dpa/s at 360 K by means of an ion irradiation of 10^{-5} dpa/s. Both neutron and ion irradiations are in the recombination domain, corresponding to case (ii) of Table III.

	Fe-P	Fe-Mn	Fe-Cr	Fe-Si	Fe-Ni	Fe-Cu
ΔT (K)	+95	+40	N/A	+90	+105	+100

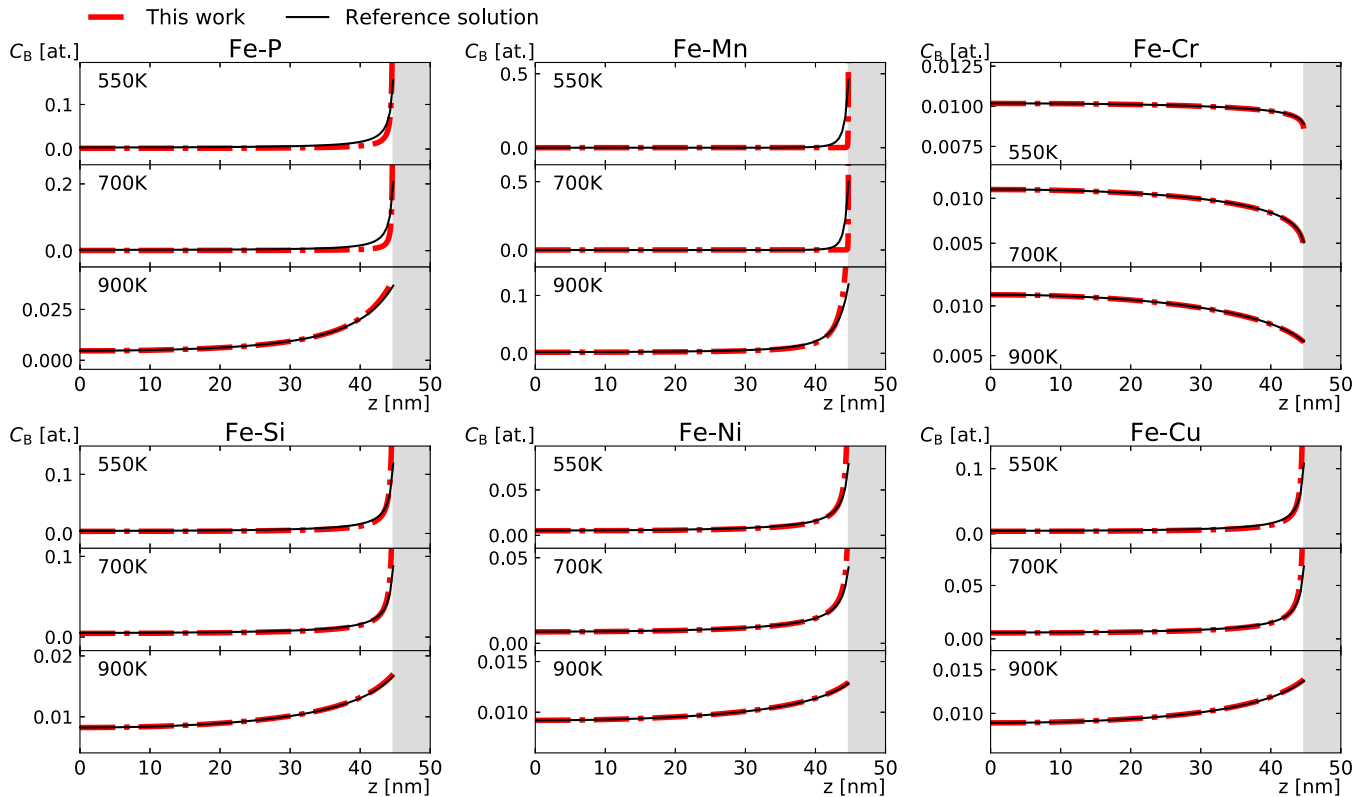


FIG. 18. Solute RIS profiles obtained by our analytical models in several dilute Fe-based alloys. The profiles obtained by the exact solution of Eq. (42) are also plotted as references. The nominal solute concentration \bar{C}_B is set to 1 at. % and the sink strength k^2 is set to 10^{15} m^{-2} . The corresponding distance between planar sinks is $h = 86 \text{ nm}$.

that the ion irradiation is in the recombination domain, we set k^2 as a linear function of $(\phi/D_V)^{0.25}$. Hence, from the simulated $k^2(\phi)$ resulting from an ion irradiation [68], we can deduce the sink strength evolution at different temperatures. Relying on our model, we calculate the evolution of S_V and S_B from the ion irradiation at different temperatures. From these results, we find out at which temperature the evolution of S_V or S_B matches well with that obtained by neutron irradiation. By this approach, we obtain the temperature shifts of an ion irradiation ($5.2 \times 10^{-5} \text{ dpa/s}$) required to emulate the RIS behaviors from neutron irradiation ($3.4 \times 10^{-7} \text{ dpa/s}$) [cf. Fig. 17(d)]. For a dose below 0.01 dpa, the temperature shift (ΔT) required for an invariant S_V is about $+90^\circ\text{C}$ and the one for an invariant S_B is about $+110^\circ\text{C}$. After 0.01 dpa, ΔT for S_V increases up to $+200^\circ\text{C}$, whereas ΔT for S_B notably decreases.

Apart from the simulation methods, direct observations of the microstructure may inform on the sink strength evolution. However, a precise estimation of the latter is difficult because, for example, small PD nanoclusters forming under irradiation are not detectable by transmission electron microscopy techniques, although complementary methods such as positron annihilation spectroscopy can provide useful information on small PD-solute clusters. Further, investigating the variation of the solute RIS profiles with radiation flux and radiation dose should give some insight on the sink strength, provided the timescale of RIS is smaller than that of the microstructure evolution, so that we may assume steady-state solute RIS. For instance, we have shown that the RIS amount of

solute atoms is directly related to the bulk concentration of vacancies. Therefore, measuring the solute RIS provides a way to estimate the bulk concentration of vacancies—thereby the global sink strength of the microstructure—provided the diffusion properties of PDs are known.

B. Major assumptions of the present RIS model and their implications

In this section, we discuss the major assumptions made in deriving the expressions of the vacancy and solute RIS profiles, and their potential impacts on the results. This discussion should highlight the limitations and possible lines of improvements of the present RIS model.

(1) To solve the PD diffusion equations, Eqs. (28) and (29), we assume that the PD diffusion coefficients D_V and D_I do not vary along the RIS profiles. This assumption is reasonable when the solute-PD interaction is weak (e.g., in Fe-Cr) or the variation of the solute concentration along the profile is small (e.g., in thermal and recombination domains). However, in the vicinity of sinks enriched in solutes, the local solute concentration could be a lot higher than the nominal one. In dilute alloys, a solute enrichment at sinks generally results from a high solute-PD attraction. The latter implies a decrease of D_V and D_I with the local solute concentration. Thus, our approach may lead to an overestimation of the PD fluxes and the RIS amount.

(2) To determine the boundary conditions, sinks are assumed to be perfect (or ideal) sinks, meaning that PD

concentration at sinks is set to its equilibrium value. However, in some cases sinks do not instantaneously absorb PDs. Then, the PD concentration at sinks may be higher than the equilibrium one, leading to smaller PD concentration gradients and fluxes. The corresponding RIS amount could be reduced and the thermal domain could be wider. Actually, the comparison between the present segregation maps and experimental observation of RIS close to the thermal regime could be a way to study the sink efficiency of structural defects.

(3) To derive the solute concentration profile from the vacancy one, the RIS factors α_1 and α_2 are assumed to be independent of the local atomic concentration C_B , although it is shown in Sec. II C 1 that this is not true in general. To check the validity of this hypothesis, we compare the RIS profiles given by the analytical model [Eq. (51)] and the corresponding reference profiles obtained from a numerical integration of Eq. (42). The numerical integration naturally accounts for the variation of α_1 and α_2 with the local solute concentration C_B . Figure 18 shows that in Fe-Cr, Fe-Si, Fe-Ni, and Fe-Cu alloys, the analytical profiles are in very good agreement with the numerical results at every temperature. In Fe-P and Fe-Mn alloys, there is a slight discrepancy between analytical and numerical RIS profiles at 550 and 700 K. Yet, the corresponding discrepancy on the solute bulk concentration and segregation amount is very small. Therefore, this assumption seems to be an appropriate one for dilute alloys.

(4) The range of FAR is restricted to 1-NN ($\sqrt{3}a_0/2$) because it has basically no influence on the transport coefficients and the short-range thermal interactions in Fe due to the relatively high thermal jump frequencies of PDs [6]. However, increasing the range of FAR could increase the backward diffusion of solute atoms close to sinks. This may decrease the solute RIS (see Fig. 16). Close to sinks, the backward diffusion is mainly determined by the FAR mechanisms. As demonstrated in Appendix C, the backward diffusion coefficient due to FAR between 1-NN is equal to $D_{\text{FAR}}^{1\text{-NN}} = a_0^2 \omega_{\text{FAR}} = n_{\text{FAR}} a_0^2 \phi$, where ω_{FAR} is the FAR frequency. Considering FAR of higher ranges, e.g., 5-NN ($\sqrt{3}a_0$), the corresponding diffusion coefficient is $D_{\text{FAR}}^{5\text{-NN}} = 4 a_0^2 \omega_{\text{FAR}} = 4 n_{\text{FAR}} a_0^2 \phi$. Thus, FAR between i -NN jumps would only change the FAR intensity by a factor Λ_i [cf. Eq. (C3)]. Therefore, we may rely on Fig. 16 to evaluate the effects of the FAR range on the solute RIS.

V. CONCLUSIONS

In this work, the cluster-expansion version of the self-consistent mean-field theory is applied to calculate the transport coefficients of dilute iron-base alloys Fe- B ($B = \text{P, Mn, Cr, Si, Ni, and Cu}$) under irradiation. We add to the recent calculation of the transport coefficients [27,47] the contribution of forced atomic relocations (FARs) [6]. From these transport coefficients, we compute the flux-coupling coefficients, the solute and vacancy diffusion coefficients, and the RIS factors with respect to temperature (T), radiation flux (ϕ), and point defect (PD) sink strength (k^2). We highlight the specificity of each alloy as well as the effect of FAR on these parameters.

We provide a general PD-RIS model yielding the concentration profile of vacancies in the vicinity of sinks in the three

kinetic domains. The profile is divided into two regions: a region of uniform vacancy concentration far from the sinks where we account for PD production, recombination, and elimination at sinks, and a second region near the PD sinks where we neglect recombination reactions because PD concentrations are lower. This approximation leads to first-order differential equations that can be solved analytically.

From the RIS factor relating the solute concentration gradient to the vacancy one, we deduce an analytical expression of the steady-state solute RIS profile. This analytical RIS model includes the full set of PD reactions, solute-PD interactions, and FAR mechanisms.

We summarize below the most relevant results obtained from an application of the analytical results to the investigated dilute Fe-based alloys.

(1) The consideration of the complete PD reactions enables a consistent investigation of RIS behaviors in all PD kinetic domains (recombination/sink/thermal). We show that the RIS kinetic domains are directly related to the PD kinetic domains, i.e., to the variation of PD concentration in the bulk. RIS profiles of PDs do not vary much with the chemical nature of the solute atom, whereas solute RIS profiles are very alloy-specific. In general, the RIS of PDs and solutes is favored in the sink domain because the rate of PD elimination at sinks is significant. In the recombination domain, even though the PD RIS amount is relatively small, the solute RIS amount can be high in certain alloys, such as in Fe-Mn where the RIS factor α_1 is relatively large.

(2) The comparison between our results and a previous study [28] highlights the sensitivity of RIS to recombination reactions. Models that would neglect these reactions would overestimate the vacancy concentration along the RIS profile, especially at low temperatures and sink strengths (i.e., in the recombination domain).

(3) Parametric T - ϕ - k^2 studies show that the effect of FAR on solute RIS is significant. At high sink strengths, FAR leads to a sharp decrease of solute RIS. Moreover, our results show that, among the investigated alloys, the effect of FAR is the most important in Fe-Ni and Fe-Cr systems.

(4) T - ϕ - k^2 maps of the RIS amount of PDs and solute atoms can be used as a tool to provide quantitative temperature-shift criteria for the comparison between neutron and ion irradiation. We emphasize that these criteria are alloy and kinetic-domain specific. In the case where we may ignore the variation of sink strength with temperature and dose rate, for instance in alloys with a high sink density, we show how to rely on the maps to deduce the temperature shifts. Otherwise, in most cases, an estimation of the temperature shift requires the knowledge of the explicit relationship between the sink strength, temperature, and dose rate.

Even though the present investigation is focused on dilute Fe-base binary alloys, the present RIS model can be applied to any alloys, provided that one is able to compute the RIS factor and the solute and PD diffusion coefficients. This RIS model can be extended to non-neutral PDs sinks by including the elastic interactions between PDs, solute atoms, and sinks into the calculation of the chemical potential gradients and the transport coefficients [48].

Finally, radiation-induced solute enrichment at sinks can exceed the alloy solubility limit and trigger the precipitation

TABLE V. Notations of the important variable.

Notation	Physical description	Expression
C_α	Local atomic composition of α	
\bar{C}_B	Nominal concentration of solute B	
C_V^b	Bulk concentration of vacancies	(18)
C_V^{eq}	Equilibrium concentration of vacancies	(19)
$d_{\alpha\beta}, d_{\alpha\beta}^c$	Partial diffusion coefficients	(10)
D_α	Diffusion coefficient of α	(12), (15)
h	Spacing between planar sinks	
k^2	Total sink strength	
k_s^2	Sink strength of sink s	
K	PD elimination rate at sinks	(21), (16)
l	Distance of the bulk regime	(36)
l_e^α	Effective width of the profile of α	(63)
$L_{\alpha\beta}$	Transport coefficients	(6)
n_{FAR}	Number of FARs per dpa	
r_c	SIA-V recombination radius	
R	SIA-V recombination rate	(21), (16)
S_α	Segregation amount of α	(39), (53)
T	Temperature	
α_1, α_2	RIS factors	(46), (47)
γ	Extent of FAR effect on solute RIS	(62)
ϕ	Dose rate/damage production rate	
Ω	Atomic volume	

of a secondary phase. Such a radiation-induced precipitation phenomenon would require different boundary conditions on the solute RIS profile, as for example a backward solute diffusion set to zero. These points are left for future work.

APPENDIX A: NOMENCLATURE

In this Appendix, we list in Table V the notations of the key variables introduced in the present work.

APPENDIX B: CALCULATION OF THE POINT DEFECT CHEMICAL POTENTIAL GRADIENT

In this Appendix, we provide details for the calculation of the point defect chemical potential gradient. For a PD ($d = V, I$), the chemical potential is given by

$$\mu_d = k_B T \ln \left(\frac{C_d}{C_d^{\text{eq}}} \right). \quad (\text{B1})$$

Thus, we have

$$\nabla \mu_d = k_B T \left(\frac{\nabla C_d}{C_d} - \frac{\nabla C_d^{\text{eq}}}{C_d^{\text{eq}}} \right). \quad (\text{B2})$$

In the infinitely dilute limit, the equilibrium concentration of d can be deduced from a low-temperature expansion formalism, i.e., Eq. (19). In this case, Eq. (B2) can be rewritten as

$$\nabla \mu_d = k_B T \left[\frac{\nabla C_d}{C_d} - \frac{(Z_{Bd} - Z_{Bd}^0) \nabla C_B}{1 + (Z_{Bd} - Z_{Bd}^0)(C_B + C_d^{\text{eq},0})} \right], \quad (\text{B3})$$

where $C_d^{\text{eq},0}$ is the equilibrium concentration of d in pure bcc iron. Note that $C_d^{\text{eq},0} \ll C_B$. Hence,

$$\nabla \mu_d = k_B T \left[\frac{\nabla C_d}{C_d} - \frac{(Z_{Bd} - Z_{Bd}^0) \nabla C_B}{1 + (Z_{Bd} - Z_{Bd}^0) C_B} \right]. \quad (\text{B4})$$

Along a RIS profile, the relative variation of C_d (up to several orders of magnitude) should be much larger than that of C_B (mostly within one order of magnitude). Therefore,

$$\frac{(Z_{Bd} - Z_{Bd}^0) \nabla C_B}{1 + (Z_{Bd} - Z_{Bd}^0) C_B} < \frac{\nabla C_B}{C_B} \ll \frac{\nabla C_d}{C_d}. \quad (\text{B5})$$

Hence, the point defect chemical potential gradient is approximated by

$$\nabla \mu_d \simeq k_B T \frac{\nabla C_d}{C_d}. \quad (\text{B6})$$

APPENDIX C: CALCULATION OF THE BACKWARD DIFFUSION COEFFICIENT CLOSE TO SINKS

In this Appendix, we give details on the calculation of the backward diffusion coefficient of solute atoms close to sinks. At realistic damage rate under irradiation (typically smaller than 1 dpa) in Fe, the FAR frequency is much smaller than the thermal jump frequencies. Thus, we may approximate the solute diffusion as the sum of the diffusion coefficients, D_{FAR} , resulting from FAR events and the thermal diffusion coefficient, D_{th} , resulting from thermal jumps of vacancies and SIAs [6]. Close to sinks, the PD concentration is very small. Since D_{th} is proportional to the PD concentration, D_{th} is small compared to D_{FAR} . The solute backward diffusion occurs close to sinks, where the solute concentration gradient is significant. Hence, we may assume that the solute backward diffusion of solute is equal to D_{FAR} .

According to the Einstein-Smoluchowski formula applied to the random walk diffusion [2], the solute backward diffusion coefficient resulting from FAR events between i -NN (i -NN FAR) is written

$$D_{\text{FAR}}^{i\text{-NN}} = \frac{\lambda_i^2 z_i \omega_{\text{FAR}}}{6} = n_{\text{FAR}} \frac{\lambda_i^2 z_i \phi}{6}, \quad (\text{C1})$$

where λ_i is the relocation distance between i -NN, z_i is the number of i -NN, and ω_{FAR} is the FAR frequency. In the present study, FAR was restricted to relocations between 1-NN, leading to $D_{\text{FAR}}^{1\text{-NN}} = n_{\text{FAR}} a_0^2 \phi$. After Eq. (C1), the change of D_{FAR} due to an increase of the relocation distance is equal to

$$D_{\text{FAR}}^{i\text{-NN}} = \Lambda_i D_{\text{FAR}}^{1\text{-NN}}, \quad (\text{C2})$$

with

$$\Lambda_i = \frac{\lambda_i^2 z_i}{\lambda_1^2 z_1}. \quad (\text{C3})$$

Therefore, i -NN FAR is equivalent to 1-NN FAR as long as the FAR intensity (n_{FAR}) entering the RIS factor α_2 [cf. Eqs. (47) and (62)] is multiplied by Λ_i . In a more general situation, the range of FAR is not unique. It may follow a probability

distribution such as the following one,

$$D_{\text{FAR}} = \sum_{i=1}^{N_m} w_i D_{\text{FAR}}^{i\text{-NN}} = \left(\sum_{i=1}^{N_m} w_i \Lambda_i \right) D_{\text{FAR}}^{\text{1NN}}, \quad (\text{C4})$$

where N_m -NN is the maximum relocation range and w_i is the probability weight of i -NN FAR events. Accordingly, this complex FAR event with multiple relocation ranges is equivalent to 1-NN FAR as long as the n_{FAR} is multiplied by $(\sum_{i=1}^{N_m} w_i \Lambda_i)$.

APPENDIX D: MATHEMATICAL DESCRIPTIONS

1. Relation between $C_V(z)$ and $C_1(z)$

Following Eq. (28) and (29), we have

$$\begin{aligned} 0 &= D_V \frac{\partial^2 C_V}{\partial z^2} - D_1 \frac{\partial^2 C_1}{\partial z^2} \\ &= \frac{\partial^2}{\partial z^2} (D_V C_V - D_1 C_1). \end{aligned} \quad (\text{D1})$$

Therefore, $D_V C_V(z) - D_1 C_1(z) = K_2 z + K_3$, with K_2 and K_3 two integration constants to be determined. By symmetry, the PD flux at the midpoint ($z = 0$) is zero; hence we have

$$\frac{\partial C_V}{\partial z}(z=0) = 0, \quad \frac{\partial C_1}{\partial z}(z=0) = 0, \quad (\text{D2})$$

and therefore $K_2 = 0$. Moreover, the PD concentrations at the sink are equal to the equilibrium concentrations. Therefore, we have

$$C_V(z = h/2) = C_V^{\text{eq}}, \quad C_1(z = h/2) = C_1^{\text{eq}}. \quad (\text{D3})$$

Using Eq. (D3), $K_3 = D_V C_V^{\text{eq}} - D_1 C_1^{\text{eq}}$. Assuming that $D_1 C_1^{\text{eq}} \ll D_V C_V^{\text{eq}}$, we get $K_3 \simeq D_V C_V^{\text{eq}}$. Accordingly, $C_V(z)$ and

$C_1(z)$ are related by

$$D_V [C_V(z) - C_V^{\text{eq}}] = D_1 C_1(z). \quad (\text{D4})$$

2. Introduction of the hypergeometric function ${}_2F_1$

The hypergeometric function ${}_2F_1(a, b, c, x)$ is defined by the series

$${}_2F_1(a, b, c, x) = \sum_{n=0}^{\infty} \frac{(a)_n (b)_n}{(c)_n n!} x^n \quad (\text{D5})$$

for $|x| \leq 1$, where $(a)_n$, $(b)_n$, and $(c)_n$ are the Pochhammer symbol [65] given by

$$(a)_n = \begin{cases} a(a+1)(a+n-1), & \text{for } n \geq 1, \\ 1, & \text{for } n = 0. \end{cases} \quad (\text{D6})$$

For $\text{Re}(c) > \text{Re}(b) > 0$, we have

$${}_2F_1(a, b, c, x) = \frac{\Gamma(c)}{\Gamma(b)\Gamma(c-b)} f(a, b, c, x), \quad (\text{D7})$$

where Γ is the Gamma function [65], and

$$f(a, b, c, x) = \int_0^1 t^{b-1} (1-t)^{c-b-1} (1-xt)^{-a} dt. \quad (\text{D8})$$

We can deduce the integral [Eq. (55)], I , from the hypergeometric function

$$\begin{aligned} I &= \left(\frac{h}{2} - l \right) b^{-2\alpha_1} \int_0^1 \left[1 - \left(\frac{h/2 - l}{b} \right)^2 t \right]^{-\alpha_1} \frac{dt}{2\sqrt{t}} \\ &= \left(\frac{h}{2} - l \right) b^{-2\alpha_1} {}_2F_1 \left(\alpha_1, \frac{1}{2}; \frac{3}{2}; \left(\frac{h/2 - l}{b} \right)^2 \right). \end{aligned} \quad (\text{D9})$$

-
- [1] K. Russell, *Prog. Mater. Sci.* **28**, 229 (1984).
 [2] G. S. Was and P. L. Andresen, *Corrosion* **63**, 19 (2007).
 [3] G. Martin and P. Bellon, *Solid State Phys.* **50**, 189 (1996).
 [4] J.-M. Roussel and P. Bellon, *Phys. Rev. B* **65**, 144107 (2002).
 [5] K. Nordlund, S. J. Zinkle, A. E. Sand, F. Granberg, R. S. Averback, R. E. Stoller, T. Suzudo, L. Malerba, F. Banhart, W. J. Weber, F. Willaime, S. L. Dudarev, and D. Simeone, *J. Nucl. Mater.* **512**, 450 (2018).
 [6] L. Huang, T. Schuler, and M. Nastar, *Phys. Rev. B* **100**, 224103 (2019).
 [7] M. Norgett, M. Robinson, and I. Torrens, *Nucl. Eng. Des.* **33**, 50 (1975).
 [8] G. Martin, *Phys. Rev. B* **30**, 1424 (1984).
 [9] K. Nordlund, S. J. Zinkle, A. E. Sand, F. Granberg, R. S. Averback, R. Stoller, T. Suzudo, L. Malerba, F. Banhart, W. J. Weber, F. Willaime, S. L. Dudarev, and D. Simeone, *Nat. Commun.* **9**, 1084 (2018).
 [10] T. R. Anthony and R. E. Hanneman, *Scr. Metall.* **2**, 611 (1968).
 [11] P. R. Okamoto and H. Wiedersich, *J. Nucl. Mater.* **53**, 336 (1974).
 [12] M. Nastar and F. Soisson, *Comprehensive Nuclear Materials* (Elsevier, Amsterdam, 2012), pp. 471–496.
 [13] A. J. Ardell and P. Bellon, *Curr. Opin. Solid State Mater. Sci.* **20**, 115 (2016).
 [14] Y. Dong, B. Sencer, F. Garner, and E. Marquis, *J. Nucl. Mater.* **467**, 692 (2015).
 [15] A. Barbu and A. J. Ardell, *Scr. Metall.* **9**, 1233 (1975).
 [16] M. K. Miller and K. F. Russell, *J. Nucl. Mater.* **371**, 145 (2007).
 [17] Y. Nishiyama, K. Onizawa, M. Suzuki, J. W. Andereg, Y. Nagai, T. Toyama, M. Hasegawa, and J. Kameda, *Acta Mater.* **56**, 4510 (2008).
 [18] M. Lambrecht and A. Almazouzi, *J. Nucl. Mater.* **385**, 334 (2009).
 [19] M. K. Miller, K. A. Powers, R. K. Nanstad, and P. Efsing, *J. Nucl. Mater.* **437**, 107 (2013).
 [20] P. D. Styman, J. M. Hyde, D. Parfitt, K. Wilford, M. G. Burke, C. A. English, and P. Efsing, *J. Nucl. Mater.* **459**, 127 (2015).
 [21] S. J. Zinkle and G. S. Was, *Acta Mater.* **61**, 735 (2013).
 [22] S. M. Bruemmer, E. P. Simonen, P. M. Scott, P. L. Andresen, G. S. Was, and J. L. Nelson, *J. Nucl. Mater.* **274**, 299 (1999).
 [23] L. Messina, M. Nastar, N. Sandberg, and P. Olsson, *Phys. Rev. B* **93**, 184302 (2016).
 [24] L. Onsager, *Phys. Rev.* **37**, 405 (1931).

- [25] H. Wu, T. Mayeshiba, and D. Morgan, *Scientific Data* **3**, 160054 (2016).
- [26] T. Schuler, D. R. Trinkle, P. Bellon, and R. Averback, *Phys. Rev. B* **95**, 174102 (2017).
- [27] L. Messina, M. Nastar, T. Garnier, C. Domain, and P. Olsson, *Phys. Rev. B* **90**, 104203 (2014).
- [28] E. Martínez, O. Senninger, A. Caro, F. Soisson, M. Nastar, and B. P. Uberuaga, *Phys. Rev. Lett.* **120**, 106101 (2018).
- [29] A. D. Marwick, *J. Phys. F: Met. Phys.* **8**, 1849 (1978).
- [30] H. Wiedersich, P. R. Okamoto, and N. Q. Lam, *J. Nucl. Mater.* **83**, 98 (1979).
- [31] C. A. English, S. M. Murphy, and J. M. Perks, *J. Chem. Soc. Faraday Trans.* **86**, 1263 (1990).
- [32] W. G. Wolfer, *J. Nucl. Mater.* **114**, 292 (1983).
- [33] Y. Grandjean, P. Bellon, and G. Martin, *Phys. Rev. B* **50**, 4228 (1994).
- [34] G. S. Was, J. T. Busby, T. Allen, E. A. Kenik, A. Jansson, S. M. Bruemmer, J. Gan, A. D. Edwards, P. M. Scott, and P. L. Andreson, *J. Nucl. Mater.* **300**, 198 (2002).
- [35] Z. Jiao, J. Michalicka, and G. S. Was, *J. Nucl. Mater.* **501**, 312 (2018).
- [36] L. Rehn, P. R. Okamoto, and H. Wiedersich, *J. Nucl. Mater.* **80**, 172 (1979).
- [37] T. R. Allen, J. I. Cole, E. A. Kenik, and G. S. Was, *J. Nucl. Mater.* **376**, 169 (2008).
- [38] L. E. Rehn, P. R. Okamoto, D. I. Potter, and H. Wiedersich, *J. Nucl. Mater.* **74**, 242 (1978).
- [39] P. Okamoto and L. Rehn, *J. Nucl. Mater.* **83**, 2 (1979).
- [40] E. Meslin, A. Barbu, L. Boulanger, B. Radiguet, P. Pareige, K. Arakawa, and C. C. Fu, *J. Nucl. Mater.* **382**, 190 (2008).
- [41] R. Sizmann, *J. Nucl. Mater.* **69–70**, 386 (1978).
- [42] L. K. Mansur, *J. Nucl. Mater.* **206**, 306 (1993).
- [43] L. Onsager, *Phys. Rev.* **38**, 2265 (1931).
- [44] M. Nastar, V. Y. Dobretsov, and G. Martin, *Philos. Mag. A* **80**, 155 (2000).
- [45] M. Nastar, *Philos. Mag.* **85**, 3767 (2005).
- [46] T. Schuler, L. Messina, and M. Nastar, *Comput. Mater. Sci.* **172**, 109191 (2020).
- [47] L. Messina, T. Schuler, M. Nastar, M.-C. Marinica, and P. Olsson, *Acta Mater.* **191**, 166 (2020).
- [48] T. Garnier, V. R. Manga, D. R. Trinkle, M. Nastar, and P. Bellon, *Phys. Rev. B* **88**, 134108 (2013).
- [49] T. Schuler, M. Nastar, and L. Messina, *Phys. Rev. Mater.* **4**, 020401(R) (2020).
- [50] T. Schuler and M. Nastar, *Phys. Rev. B* **93**, 224101 (2016).
- [51] V. Barbe and M. Nastar, *Philos. Mag.* **87**, 1649 (2007).
- [52] V. Barbe and M. Nastar, *Phys. Rev. B* **76**, 054206 (2007).
- [53] F. Ducastelle, in *Order and Phase Stability in Alloys* (North Holland, Amsterdam, 1991).
- [54] T. Schuler, M. Nastar, and F. Soisson, *Phys. Rev. B* **95**, 014113 (2017).
- [55] T. Schuler, P. Bellon, D. R. Trinkle, and R. S. Averback, *Phys. Rev. Mater.* **2**, 073605 (2018).
- [56] T. R. Anthony, *Acta Metall.* **17**, 603 (1969).
- [57] T. R. Anthony, *J. Appl. Phys.* **41**, 3969 (1970).
- [58] H. Davis, *Introduction to Nonlinear Differential and Integral Equations* (Dover, New York, 1962).
- [59] N. Q. Lam, S. J. Rothman, and R. Sizmanns, *Radiat. Eff.* **23**, 53 (1974).
- [60] H. Rauh, M. H. Wood, and R. Bullough, *Philos. Mag. A* **44**, 1255 (1981).
- [61] F. A. Nichols, *J. Nucl. Mater.* **75**, 32 (1978).
- [62] S. M. Foiles, *Phys. Rev. B* **40**, 11502 (1989).
- [63] M. Menyhard, M. Yan, and V. Vitek, *Acta Metall. Mater.* **42**, 2783 (1994).
- [64] J. Creuze, F. Berthier, R. Tétot, and B. Legrand, *Phys. Rev. B* **62**, 2813 (2000).
- [65] G. E. Andrews, R. Askey, and R. Roy, *Special Functions* (Cambridge University Press, Cambridge, 1999).
- [66] A. J. E. Foreman, *Radiat. Eff.* **14**, 175 (1972).
- [67] F. Soisson and T. Jourdan, *Acta Mater.* **103**, 870 (2016).
- [68] F. Soisson, E. Meslin, and O. Tissot, *J. Nucl. Mater.* **508**, 583 (2018).